

Synthesis, structure, linear and nonlinear optical properties of  
noncentrosymmetric quaternary diamond-like semiconductors,  $\text{Cu}_2\text{ZnGeSe}_4$   
(CZGSe) and the novel  $\text{Cu}_4\text{ZnGe}_2\text{Se}_7$ .

Charles W. Sinagra III,<sup>1</sup> Felix O. Saouma,<sup>2</sup> Calford O. Otieno,<sup>3</sup> Saul H. Lapidus,<sup>4</sup> Jian-Han Zhang,<sup>5</sup>  
Andrew J. Craig,<sup>1</sup> Pedro Grima-Gallardo,<sup>6,7</sup> Jacilynn A. Brant,<sup>1</sup> Kimberly A. Rosmus,<sup>1</sup> Kate E.  
Rosello,<sup>1</sup> Joon I. Jang,<sup>8\*</sup> Jennifer A. Aitken<sup>1\*</sup>

<sup>1</sup>Department of Chemistry and Biochemistry, Duquesne University, Pittsburgh PA 15282, USA

<sup>2</sup>Department of Physical Sciences, Kaimosi Friends University College, P.O. Box: 385-50309,  
Kaimosi, Kenya

<sup>3</sup>Department of Physics, Kisii University, P.O. Box: 405, Kisii, Kenya

<sup>4</sup>X-ray Science Division, Advanced Photon Source, Argonne National Laboratory, Argonne, IL  
60439, USA.

<sup>5</sup>School of Resources and Chemical Engineering, Sanming University, Sanming, 365004, P.R.  
China

<sup>6</sup>Centro de Estudios en Semiconductores (CES), Departamento de Física, Facultad de Ciencias,  
Universidad de Los Andes (ULA), Mérida, Venezuela.

<sup>7</sup>Centro Nacional de Tecnología Óptica (CNTO), Mérida, Venezuela

<sup>8</sup>Department of Physics, Sogang University, Seoul 04017, South Korea

\*Co-corresponding authors – [jjcoupling@sogang.ac.kr](mailto:jjcoupling@sogang.ac.kr), [aitkenj@duq.edu](mailto:aitkenj@duq.edu)

## Abstract:

In this study, two quaternary diamond-like semiconductors (DLSs) in the Cu-Zn-Ge-Se system, the known  $\text{Cu}_2\text{ZnGeSe}_4$  (also referred to as CZGSe) and the new  $\text{Cu}_4\text{ZnGe}_2\text{Se}_7$ , are compared in terms of their crystal structures, electronic structures and physicochemical properties. Both compounds were prepared by high-temperature, solid-state synthesis at  $800^\circ\text{C}$ . Single crystal X-ray diffraction was used to determine the structure of  $\text{Cu}_4\text{ZnGe}_2\text{Se}_7$ . The structures of both  $\text{Cu}_2\text{ZnGeSe}_4$  and  $\text{Cu}_4\text{ZnGe}_2\text{Se}_7$  can be considered as derivatives of cubic diamond.  $\text{Cu}_4\text{ZnGe}_2\text{Se}_7$ , with a reduced symmetry due to the cation ordering pattern, adopts the  $\text{Cu}_4\text{NiSi}_2\text{S}_7$  structure type, with space group  $C2$ . The corner-sharing tetrahedra in  $\text{Cu}_4\text{ZnGe}_2\text{Se}_7$  are slightly distorted because the charge for some of the  $\text{S}^{2-}$  anions is not compensated by the first-nearest-neighbor cations. Rietveld refinements using synchrotron X-ray powder diffraction data were used to assess the phase purity of the samples and confirm the bulk structural behavior. Diffuse reflectance UV/Vis/NIR spectroscopy shows that  $\text{Cu}_2\text{ZnGeSe}_4$  and  $\text{Cu}_4\text{ZnGe}_2\text{Se}_7$  have direct optical bandgaps of 1.38 and 0.91 eV, respectively. Electronic structure calculations implementing density function theory confirm the direct bandgap for  $\text{Cu}_4\text{ZnGe}_2\text{Se}_7$ , with a calculated value of 0.62 eV. Both compounds are air stable, thermally stable up to relatively high temperatures, undergo phase transitions and have wide windows of optical clarity. The Kurtz-Perry powder technique was used to determine the second harmonic generation (SHG) responses using a commercial  $\text{AgGaSe}_2$  standard. While  $\text{Cu}_4\text{ZnGe}_2\text{Se}_7$  displays a weak SHG response,  $\text{Cu}_2\text{ZnGeSe}_4$  exhibits a response that is greater than several benchmark materials, with a large SHG coefficient,  $\chi^{(2)}$ , of  $43 \pm 6$  pm/V at  $\lambda = 2900$  nm.

Keywords: inorganic materials; crystal structure; nonlinear optics; X-ray diffraction; optical properties

## 1. Introduction

Nonlinear optical (NLO) materials serve many purposes, such as wavelength converters and optical amplifiers, in the ultraviolet (UV) to the terahertz (TZ) regimes. In particular, there is a great demand for infrared (IR) NLO materials, which have many important military, medical and environmental applications. For example, current IR counter measure systems attached to military aircraft employ ZnGeP<sub>2</sub> (ZGP) optical parametric oscillators (OPOs)[1]. Trace detection of explosive vapors and chemical warfare agents can be carried out in the field using all solid-state laser systems with wavelengths generated by IR NLO crystals [2]. New devices employing different wavelengths for high-precision laser surgery have been explored to minimize collateral damage to surrounding healthy tissue and to quicken patient recovery times [3]. Analysis of breath biomarkers using molecular spectroscopy can be exploited for noninvasive medical diagnostics and monitoring [4]. Additionally, trace sensing of atmospheric gas pollutants can also be carried out using molecular spectroscopy devices [5]. Despite all of these and many other uses, there is a scarcity of ideal IR NLO materials.

Like many fields of materials science, nonlinear optics is an area where the model material must simultaneously meet a number of complex criteria, some of which are negatively correlated [6]. A desirable NLO material should exhibit extreme optical transparency in the region of intended use, adequate birefringence for phase matching (PM), a large NLO coefficient, high laser-induced damage threshold (LIDT), high thermal conductivity, environmental stability and adequate mechanical properties that allow for cutting and polishing, among others. Moreover, researchers must be able to grow large, crack-free single crystals of the material with minimal absorption losses [7,8].

The current commercially available IR NLO crystals, most of which belong to the family of diamond-like semiconductors (DLSs), have both strengths and weaknesses. ZGP has an extremely high second-order NLO coefficient,  $\chi^{(2)}$ , of 150 pm/V; however, it suffers from multiphoton absorption (MPA) effects around 8.5  $\mu\text{m}$  [9]. While AgGaSe<sub>2</sub> (AGSe) can be used at longer wavelengths than ZGP, with transparency from the visible out to 19  $\mu\text{m}$  [10], it is nonphasematching (non-PM) at 1  $\mu\text{m}$  [8]. AgGaS<sub>2</sub> (AGS) is transparent and PM at 1  $\mu\text{m}$  [8], yet it has a lower  $\chi^{(2)}$  than that of ZGP and AGSe [7]. Furthermore, the large-scale crystal growth for all of the commercially available IR NLO materials is nontrivial. Thus, a search for improved materials is warranted.

While many researchers have been looking for new, next-generation IR NLO crystals among chalcogenides [11-24], our design strategy has been to specifically target quaternary chalcogenides with diamond-like structures because their compositions are predictable [25-28], their structures are inherently noncentrosymmetric, and they have demonstrated sizeable second harmonic generation (SHG) responses. Indeed, several outstanding quaternary DLSs with a good balance of  $\chi^{(2)}$  and LIDT have been recently identified by our group and others, for example Li<sub>2</sub>MnGeS<sub>4</sub> [29], Li<sub>2</sub>ZnSiS<sub>4</sub> [30],  $\alpha$ -Li<sub>2</sub>ZnGeS<sub>4</sub> [31],  $\beta$ -Li<sub>2</sub>ZnGeS<sub>4</sub> [32], Li<sub>2</sub>CdSiS<sub>4</sub> [33,34], Li<sub>2</sub>CdGeS<sub>4</sub> [35], Li<sub>4</sub>CdSn<sub>2</sub>S<sub>7</sub> [33], Li<sub>2</sub>HgSiS<sub>4</sub> [36] and Li<sub>4</sub>HgGe<sub>2</sub>S<sub>7</sub> [37].

In spite of the recent discoveries of promising DLSs, the relationships between structure, composition and properties in these systems are still being developed. Additionally, researchers are continually striving to achieve the best balance between the characteristics of the requisite materials. Currently, the nonlinear optical properties of many known diamond-like chalcogenides have not been studied. Additionally, there are still many DLSs that have yet to be discovered. In this paper, we report on two such compounds.  $\text{Cu}_2\text{ZnGeSe}_4$  (also referred to as CZGSe) is a known,  $\text{I}_2\text{-II-IV-VI}_4$  DLS first reported in 1960s [38, 39] that has recently been evaluated for use in solar cells [40,41] and thermoelectric applications [42,43], yet its NLO properties have not been investigated until now.  $\text{Cu}_4\text{ZnGe}_2\text{Se}_7$  is a novel DLS of the  $\text{I}_4\text{-II-IV}_2\text{-VI}_7$  family, for which there exist only a few members, [33,37,44-48]. Here we present the synthesis, crystal structure, thermal analysis, optical bandgaps, IR transparency and SHG for these two DLSs. Electronic structure calculations have also been carried out for  $\text{Cu}_4\text{ZnGe}_2\text{Se}_7$  and compared to those previously published for  $\text{Cu}_2\text{ZnGeSe}_4$  [49-52].

## 2. Materials and Methods

### 2.1 Reagents

Copper powder (99.999%), germanium powder (99.999%), selenium powder (99.99%), and zinc powder (99.999%), all purchased from Strem (Newburyport, MA), were used without further purification.

### 2.2 Synthesis

Stoichiometric amounts of the elemental reagents, with the exception of selenium that was added in 5% excess, were weighed and combined (not ground) in an argon-filled glovebox in order to make ca. 2 mmol of product. The reagent mixtures were placed into small, ~5 cm long, 9 mm o.d. fused-silica tubes, which were subsequently inserted into longer, ~18 cm long, 12 mm o.d. fused-silica tubes. The tubes were removed from the glovebox, connected to a vacuum line, evacuated to a pressure of  $\sim 10^{-3}$  mbar and sealed to an approximate length of 10 cm using an oxy-methane torch. The reaction vessels were inserted into computer-controlled furnaces. For  $\text{Cu}_2\text{ZnGeSe}_4$ , the reaction vessel was heated to 800 °C at a rate of 65 °C h<sup>-1</sup>, held at that temperature for eight days, cooled to 400 °C at a rate of 7.5 °C h<sup>-1</sup> and subsequently cooled to room temperature ambiently. In the case of  $\text{Cu}_4\text{ZnGe}_2\text{Se}_7$ , the same heating profile was conducted with the exception that the hold time at 800 °C was only four days. After the reaction, the tubes were split open and the contents were inspected under an optical microscope. The products were grayish-black microcrystalline powders. Needle-like and irregular polyhedral-shaped crystals on the order of tens to several hundred  $\mu\text{m}$  on an edge were observed. Single crystals of  $\text{Cu}_4\text{ZnGe}_2\text{Se}_7$  were selected for single crystal X-ray diffraction and the rest of the samples were ground to fine powders for subsequent characterization. Both compounds are air and moisture stable.

## 2.3 Physical Property Measurements

### 2.3.1 Single Crystal X-ray Diffraction

A dark, needle-like single crystal, having dimensions of 0.23 x 0.03 x 0.02 mm, was selected under an optical microscope and mounted to a glass fiber using Krazy™ glue. Using the SMART software, diffraction data were collected for 40 s per frame at room temperature on a Bruker Smart APEX2 CCD single crystal X-ray diffractometer operating with a tube power of 50 kV and 40 mA under Mo  $K_{\alpha}$  radiation. Data reduction and the final unit cell refinement were carried out using SAINT [53]. The absorption correction was performed via SADABS and files were generated for SHELX using XPREP [54a]. The structure was solved by direct methods and refined as a racemic twin using SHELXL97 [54b]. The final Flack parameter was refined to 0.10(3), indicating the correct absolute structure. It should be noted that the systematic absences indicated three possible space groups,  $C2$ ,  $Cm$  and  $C2/m$ ; however, the structure could only be solved and refined in  $C2$ . The noncentrosymmetric space group was expected, because all DLSs are inherently noncentrosymmetric, and confirmed by the SHG response. Full and abbreviated lists of crystallographic data, data collection parameters and structure refinement details for  $Cu_4ZnGe_2Se_7$  are given in Table S1 and Table 1, respectively. Atomic coordinates, atomic displacement parameters, bond distances, and bond angles are given in Tables S2-S5. The CIF file is deposited with the Cambridge Structural Database, CSD 2098273.

### 2.3.2 Synchrotron X-ray Powder Diffraction and Rietveld Refinement

High-resolution synchrotron X-ray powder diffraction data for  $Cu_2ZnGeSe_4$  and  $Cu_4ZnGe_2Se_7$  were collected at room temperature using an energy of 27 keV, wavelength of 0.4590 Å, at the high-resolution powder diffractometer, beamline 11-BM, of the Advanced Photon Source at Argonne National Laboratory. Details of the instrumental setup have been described elsewhere [55].

Rietveld refinements were performed utilizing TOPAS Academic v6 [56]. Both the stannite-type structure determined by Parasyuk *et al.* [57] and the kesterite-type structure [58] were used as the starting models in the case of the  $Cu_2ZnGeSe_4$  sample. The kesterite-type structure with a moderate degree of Cu-Zn disorder was more recently established by Schorr and her team by applying an average neutron scattering length analysis [58]. The data collected for the  $Cu_4ZnGe_2Se_7$  sample was fit well with a two-phase model using the single crystal X-ray structure reported here and the structure determined by Schorr and coworkers [58] for  $Cu_4ZnGe_2Se_7$  (major phase) and  $Cu_2ZnGeSe_4$  (minor phase), respectively. However, due to X-ray diffraction techniques not being sensitive to the difference between Cu and Zn, attributable to their similar X-ray scattering cross-sections, we cannot rule out the structure proposed by Parasyuk [57]. The model used by Schorr's group [58] was chosen due to that model being based on neutron diffraction, which is sensitive to the differences of Cu and Zn. Lattice parameters, atomic coordinates and isotropic displacement parameters were refined for both sets of data and

phase fractions were additionally refined for the sample that was primarily  $\text{Cu}_4\text{ZnGe}_2\text{Se}_7$ . Selected Rietveld refinement details for both samples are provided in Tables S6 and S7.

### 2.3.3 Sample Morphology and Elemental Analysis

#### 2.3.3.1 Scanning Electron Microscopy (SEM) and Energy Dispersive Spectroscopy (EDS)

Samples were prepared for SEM by pressing crystals onto double-sided carbon tape that was attached to an aluminum specimen holder. Secondary electron images of the crystals were obtained using a Hitachi S-3400N scanning electron microscope operating with an accelerating voltage of 5 kV. The SEM was equipped with a Bruker Quantax model 400 energy dispersive spectrometer that uses an XFlash 5010 EDS detector. To collect semi-quantitative energy dispersive spectroscopy data, the accelerating voltage, data collection time and working distance were set to 15 kV, 5 min live time and 10 mm, respectively. Multiple measurements were obtained for the crystals and the results were averaged.

#### 2.3.3.2 Inductively Coupled Plasma Optical Emission Spectroscopy (ICP-OES)

Quantitative elemental analysis via ICP-OES was performed by RJ Lee Group Inc. in Monroeville, PA. For each compound, 50 mg of sample was prepped for ICP-OES using a standard microwave-assisted acid digestion protocol in high-pressure XP1500 vessels with a MARS Xpress CEM Microwave system. After digestion, the samples were evaluated for Cu, Zn, Ge and Se using a Varian 730ES ICP-OES.

#### 2.3.4 Differential Thermal Analysis (DTA)

Roughly 20 mg of each sample was added to a carbon-coated, fused-silica ampoule and flame-sealed at  $\sim 10^{-3}$  mbar. For each sample, another ampoule containing an alumina reference of comparable mass was prepared. Alumina is used as the reference material because it does not undergo any thermal events in the investigated temperature range. Data were collected using a Shimadzu DTA50 differential thermal analyzer that was calibrated using a three-point calibration curve. Under the flow of  $\text{N}_2$ , the sample and the reference were heated from room temperature to 1000 °C at a rate of 10 °C  $\text{min}^{-1}$ , held at 1000 °C for 1 min and cooled to 100 °C at the same rate. This heating profile was continuously carried out in duplicate in order to ascertain the reversibility of the thermal events.

#### 2.3.5 Diffuse Reflectance UV/Vis/NIR Spectroscopy

To prepare for measurements, each of the ground samples was pressed onto a compacted barium sulfate standard (100% reflectance) that was preloaded into the sample cup. Diffuse reflectance data were collected using a Varian Cary 5000 with the Harrick praying mantis attachment. Data were collected from 2500 nm to 200 nm, which corresponds to approximately 0.5-6.2 eV, at a scan speed of 600 nm  $\text{min}^{-1}$ . Using the Kubelka-Munk transformation,  $\alpha_{\text{KM}}/s = (1-R)^2/(2R)$ , the raw reflectance ( $R$ ) data were converted to relative

absorption ( $\alpha_{KM}$ ), since the scattering coefficient,  $s$ , is unknown [59]. The Urbach energy was obtained using the functional form  $\alpha = A \cdot \exp[(E-E_g)/E_u]$ , where  $A$  is a constant,  $E$  is the photon energy in eV,  $E_g$  is the band gap energy, and  $E_u$  is the Urbach energy [60].

### 2.3.6 Attenuated Total Reflectance (ATR) Fourier Transform Infrared (FT-IR) Spectroscopy

Data were collected with a Thermo Nicolet 380 FT-IR spectrometer outfitted with an attenuated total reflectance (ATR) accessory. The spectra are made up of 64 scans, from 400  $\text{cm}^{-1}$  to 4000  $\text{cm}^{-1}$ . This FT-IR set up utilized a diamond crystal that is in optical contact with the sample; therefore, the depth of penetration into the sample is approximately 2  $\mu\text{m}$  and near the lower limit of the sample particle size. This renders the effect of thickness dependence on the intensity of the obtained spectrum insignificant [61].

### 2.3.7 Second Harmonic Generation (SHG)

Approximately two grams of  $\text{Cu}_2\text{ZnGeSe}_4$  and  $\text{Cu}_4\text{ZnGe}_2\text{Se}_7$  were prepared for SHG measurements by sieving the microcrystalline powders into specific particle-size ranges with diameters ( $d$ ) of < 20  $\mu\text{m}$ , 20-45  $\mu\text{m}$ , 45-63  $\mu\text{m}$ , 63-75  $\mu\text{m}$ , 75-90  $\mu\text{m}$ , 90-106  $\mu\text{m}$ , 106-125  $\mu\text{m}$ , and 125-150  $\mu\text{m}$ , to examine the PM behavior of the samples [62]. The powders of distinct particle-size ranges were closed up in fused-silica tubes to preclude exposure to air and moisture during experiments. Each tube was lodged into a homemade sample holder that was subsequently mounted on a Z-scan translation stage. The SHG efficiencies of the samples were directly compared with that of AGSe, a benchmark reference material that was obtained by grinding an optical-quality single crystal, obtained from G&H Cleveland, to a powder and preparing discrete particle-size ranges, as described above for the samples under investigation.

Wavelength-dependent SHG responses were determined at ambient temperature conditions. To irradiate broadband tunable laser pulses, coherent light of 1064 nm was first produced using an EKSPLA PL-2250 series diode-pumping picosecond Nd:YAG laser with a pulse width of 30 ps and a repetition rate of 50 Hz. The Nd:YAG laser pumped an EKSPLA Harmonics Unit (HU) H400, where the input beam was frequency tripled by a successive cascade of NLO wave mixing. The 1064 nm and frequency-tripled radiation (355 nm) from the HU entered an EKSPLA PG403-SH-DFG OPO composed of four main parts: a double pass parametric generator, a single-pass parametric amplifier, a second harmonic generator and a difference frequency generator [63]. The selected output fundamental wavelengths used in the experiments ranged from 2900 nm to 3900 nm in 200 nm increments. SHG at lower wavelengths was not measured because of the narrow bandgaps of the samples and thus absorption of the beam. The measured SHG wavelength, half the fundamental wavelength, corresponds to  $\lambda_{\text{SHG}} = 1450\text{-}1950$  nm.

The incident pulse energy was tuned to 10  $\mu\text{J}$  before being delicately focused onto the samples with a spot size of  $\sim 0.5$  mm in diameter by a  $\text{CaF}_2$  lens ( $f = 75$  mm) far away from the Z-scan focus to avoid sample damage. The SHG signal from the samples was collected using a reflection geometry by a fiber-optic bundle, which was coupled to a selective-grating

spectrometer, set to 300 grooves/mm and equipped with an InGaAs IR detector. The spectrally resolved SHG responses at each fundamental wavelength were accurately calibrated with the known and measured quantum efficiencies of the system.

## 2.4 Electronic Structure Calculations

Electronic structure calculations, including the electronic band structure, total density of states (DOS) and partial density of states (pDOS) for  $\text{Cu}_4\text{ZnGe}_2\text{Se}_7$  were performed with the CASTEP program [64]. CASTEP implements the plane-wave pseudopotential method within density function theory to calculate the total energy using the Kohn-Sham equations [65]. The Perdew-Burke-Ernzerhof generalized gradient approximation (PBE-GGA) was used to treat the exchange and correlation effects [66]. In this method, the interactions between the ionic cores and the electrons are described by norm-conserving pseudopotentials to allow for proper numerical convergence [67]. The following configurations,  $3p^63d^{10}4s^1$ ,  $3p^63d^{10}4s^2$ ,  $4s^24p^2$  and  $4s^24p^4$ , were considered as the valence electrons for copper, zinc, germanium and selenium, respectively. An energy cutoff of 800 eV was used to establish the number of plane-waves comprising the basis set. The numerical integration of the Brillouin zone was performed using a  $3 \times 3 \times 3$  Monkhorst-Pack  $k$ -point sampling in reciprocal space. Convergence for the total energy was attained when the difference between iterations was  $1 \times 10^{-6}$  eV atom<sup>-1</sup> in the self-consistent field (SCF). For the other parameters, the suggested values given in the CASTEP program were utilized. The single crystal X-ray structure for  $\text{Cu}_4\text{ZnGe}_2\text{Se}_7$  obtained in this study was used as input.

## 3. Results and Discussion

Table 1. Select crystallographic data and structure refinement details for  $\text{Cu}_4\text{ZnGe}_2\text{Se}_7$ .

Formula weight	1017.43
Temperature (K)	296(2)
$\lambda$ (Å)	0.71073
Space group	C2 (No. 5)
$a$ (Å)	12.3443(4)
$b$ (Å)	5.6195(2)
$c$ (Å)	8.7904(3)
$\beta$ (°)	98.693(2)
$V$ (Å <sup>3</sup> )	602.77(4)
$Z$	2
Density (g cm <sup>-3</sup> )	5.606
$\mu$ (mm <sup>-1</sup> )	34.875
Reflections collected/unique	4254/1344
GOF on $F^2$	1.079
Absolute structure parameter	0.10(4)
$R1, wR2$ [ $I > 2\sigma(I)$ ]	0.0301, 0.0778
$R1, wR2$ (all data)	0.0337, 0.0808
Peak and hole (e Å <sup>-3</sup> )	0.834, -1.333

### 3.1 Crystal Structure

While earlier reports of  $\text{Cu}_2\text{ZnGeSe}_4$  reported it to crystallize in the stannite structure type with space group  $I-42m$  (No. 121) [38,39,57,68-71], more recent Raman [72] and neutron diffraction [58] studies indicate that  $\text{Cu}_2\text{ZnGeSe}_4$  crystallizes with the kesterite-structure type in the tetragonal space group  $I-4$  (No. 82).  $\text{Cu}_4\text{ZnGe}_2\text{Se}_7$  is a new compound with the more complex  $\text{Cu}_4\text{NiSi}_2\text{S}_7$  structure type [44] crystallizing in the monoclinic space group  $C2$ . Below the structure of  $\text{Cu}_4\text{ZnGe}_2\text{Se}_7$  will be described in detail and compared to both the stannite and kesterite structures reported for  $\text{Cu}_2\text{ZnGeSe}_4$ .

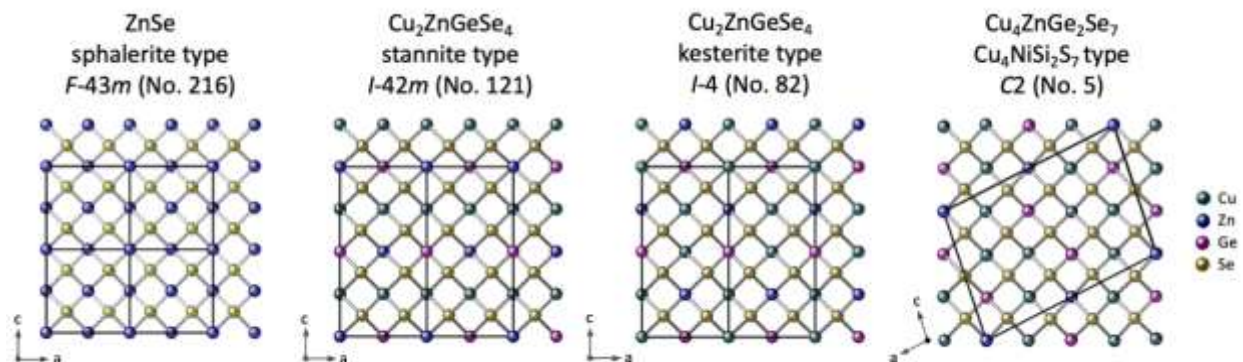


Figure 1. The crystal structures of sphalerite-type  $\text{ZnSe}$ , stannite-type  $\text{Cu}_2\text{ZnGeSe}_4$ , kesterite-type  $\text{Cu}_2\text{ZnGeSe}_4$  and  $\text{Cu}_4\text{ZnGe}_2\text{Se}_7$  displayed from left to right (from higher symmetry to lower symmetry) and viewed along the crystallographic  $b$  axes. All four structures can be considered derivatives of cubic diamond, space group  $Fd-3m$  (No. 227). As more cations are incorporated and the cation ordering pattern becomes more complex, the unit cells grow larger and the symmetry drops from cubic to tetragonal to monoclinic, from left to right. It should be noted that the  $C2$  space group is a subgroup of  $I-4$ , which is a subgroup of  $I-42m$ .

The structure of  $\text{Cu}_4\text{ZnGe}_2\text{Se}_7$  contains eight crystallographically unique atoms, two copper, one zinc, one germanium and four selenium. All atoms are located on general positions with the exception of the Zn and Se1 atoms that lie on two-fold axes, sites  $2a$  and  $2b$ , respectively. Figure 1 shows the structure of  $\text{Cu}_4\text{ZnGe}_2\text{Se}_7$  in comparison to sphalerite-type  $\text{ZnSe}$  [73] and both structure types reported for  $\text{Cu}_2\text{ZnGeSe}_4$ , viewed along the  $b$  axis. Sphalerite-type  $\text{ZnSe}$  can be considered as a derivative of the cubic diamond structure where the carbon atoms have been replaced with  $\text{Zn}^{2+}$  cations and  $\text{Se}^{2-}$  anions in an organized fashion, such that every cation is surrounded by four anions and vice versa. Upon going from cubic  $\text{ZnSe}$  to  $\text{Cu}_2\text{ZnGeSe}_4$ , three cations are distributed over the Zn site of sphalerite, the unit cell doubles in the  $c$ -direction and the symmetry drops from cubic to tetragonal, due to the different metal-Se bond distances. A relatively simple cation ordering pattern exists in  $\text{Cu}_2\text{ZnGeSe}_4$ . For the stannite type there are rows of  $\text{Cu}^{1+}$  cations separated by rows of alternating  $\text{Zn}^{2+}$  and  $\text{Ge}^{4+}$  along the  $a$ -axis. For the kesterite type there are rows of alternating  $\text{Ge}^{4+}$  and  $\text{Cu}^{1+}$  separated by rows of alternating  $\text{Zn}^{2+}$  and  $\text{Cu}^{2+}$  along the  $a$ -axis. It should be noted that in the kesterite structure model a moderate degree of Cu-Zn disorder was noted by Schorr and her team [58]; <15% Zn resides on the mainly copper,  $2c$ , site and <15% Cu sits on the predominantly Zn,  $2d$ , site. The cation ordering pattern in  $\text{Cu}_4\text{ZnGe}_2\text{Se}_7$  is more complicated, Figure 1. Due to the different stoichiometry and, therefore, more intricate cation-ordering pattern, the unit cell volume of  $\text{Cu}_4\text{ZnGe}_2\text{Se}_7$  is  $\sim 1.7x$  that of  $\text{Cu}_2\text{ZnGeSe}_4$ .

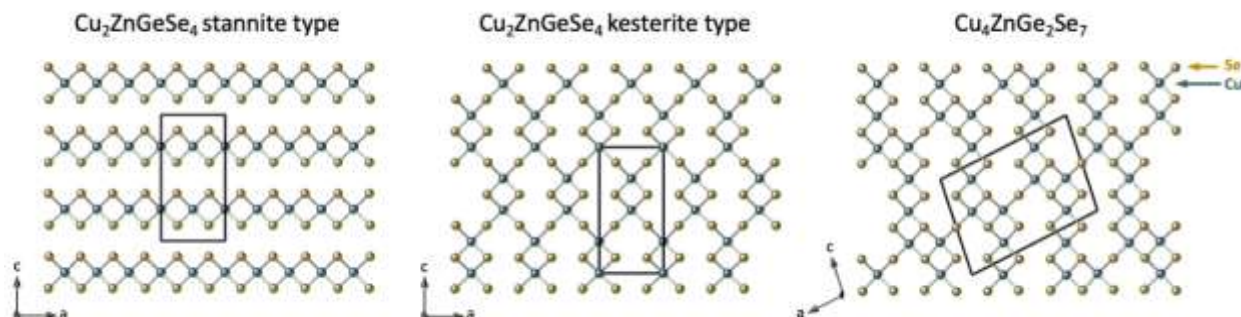


Figure 2. The Cu-Se frameworks in stannite-type  $\text{Cu}_2\text{ZnGeSe}_4$ , kesterite-type  $\text{Cu}_2\text{ZnGeSe}_4$  and  $\text{Cu}_4\text{ZnGe}_2\text{Se}_7$  displayed from left to right and viewed along the crystallographic  $b$  axes. The zinc and germanium atoms have been omitted for clarity. The  $\text{CuSe}_4$  tetrahedra share corners to form layers in the  $ab$  plane for stannite-type  $\text{Cu}_2\text{ZnGeSe}_4$  and a three-dimension framework in the cases of kesterite-type  $\text{Cu}_2\text{ZnGeSe}_4$  and  $\text{Cu}_4\text{ZnGe}_2\text{Se}_7$ .

The structures of  $\text{Cu}_2\text{ZnGeSe}_4$  (either stannite or kesterite type) and  $\text{Cu}_4\text{ZnGe}_2\text{Se}_7$  can be thought of as distorted “cubic closest-packed” arrays of  $\text{Se}^{2-}$  anions in which the cations,  $\text{Cu}^+$ ,  $\text{Zn}^{2+}$  and  $\text{Ge}^{4+}$  occupy  $\frac{1}{2}$  of the tetrahedral holes. In these structures the  $\text{ZnSe}_4$  tetrahedra are isolated from one another. The  $\text{GeSe}_4$  tetrahedra are also isolated from one another in both the stannite- and kesterite-type  $\text{Cu}_2\text{ZnGeSe}_4$ ; however, in the case of  $\text{Cu}_4\text{ZnGe}_2\text{Se}_7$ , two  $\text{GeSe}_4$  units share a corner to create  $(\text{Ge}_2\text{Se}_7)^{6-}$  dimers. The  $\text{CuSe}_4$  tetrahedra alone create a three-dimensional network in both kesterite-type  $\text{Cu}_2\text{ZnGeSe}_4$  and  $\text{Cu}_4\text{ZnGe}_2\text{Se}_7$ , Figure 2. This in contrast to the stannite structure, where the  $\text{CuSe}_4$  tetrahedra form layers in the  $ab$  plane. The corner-sharing network of tetrahedra in both  $\text{Cu}_2\text{ZnGeSe}_4$  and  $\text{Cu}_4\text{ZnGe}_2\text{Se}_7$  gives rise to noncentrosymmetric structures, because all of the tetrahedra are aligned along one crystallographic direction, Figure 3.

Pauling’s second rule [74] states that the charge of each anion in the structure should be compensated by the valence bonds of the nearest neighbor cations in order for regular coordination polyhedra to exist. This is the case in both the kesterite- and stannite-type structures of  $\text{Cu}_2\text{ZnGeSe}_4$ , while some of the selenide ions in  $\text{Cu}_4\text{ZnGe}_2\text{Se}_7$  do not have their charge compensated within the first coordination sphere. Pauling’s second rule goes on to predict that in this situation, the structures will undergo some distortions; metal-anion bonds will lengthen in the case of anions that are overcompensated in terms of charge and shortened for those that are undercompensated. Of the four crystallographically unique selenium atoms in  $\text{Cu}_4\text{ZnGe}_2\text{Se}_7$ , only Se2 and Se4 have their charge compensated by first-nearest neighbors, Figure 4. Both Se2 and Se4 are bound to two  $\text{Cu}^+$ , one  $\text{Zn}^{2+}$  and one  $\text{Ge}^{4+}$ . Because each of these cations is also connected to three other selenium atoms, the charge of the first nearest neighbors surrounding Se2 and Se4 sums up to 2 ( $1/4 + 1/4 + 2/4 + 4/4 = 2$ ). Therefore, the net charge on Se2 and Se4 is zero. This local charge neutrality suggests that metal-Se2 and metal-Se4 bond distances will be more-or-less regular. In contrast, the Se1 atom is connected to two Cu1 atoms and two Ge atoms and its charge is overcompensated by +0.5. On the other hand, the Se3 atom has, two Cu1, one Cu2 and one Ge atom in its first coordination sphere, resulting in an undercompensation of charge by -0.25. For Se1 and Se3, Pauling’s second rule predicts a lengthening and shortening of the bonds, respectively.

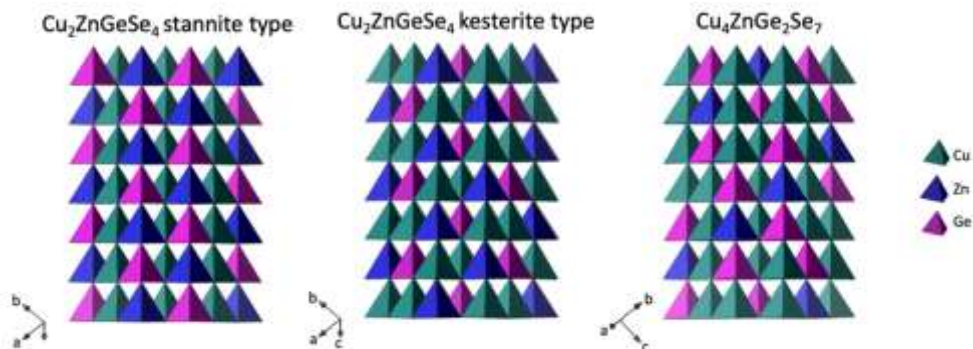


Figure 3. Polyhedral representation of stannite-type  $\text{Cu}_2\text{ZnGeSe}_4$ , kesterite-type  $\text{Cu}_2\text{ZnGeSe}_4$  and  $\text{Cu}_4\text{ZnGe}_2\text{Se}_7$ , displayed from left to right, demonstrating the lack of an inversion center in these structures, as all tetrahedra are aligned along the same crystallographic direction.

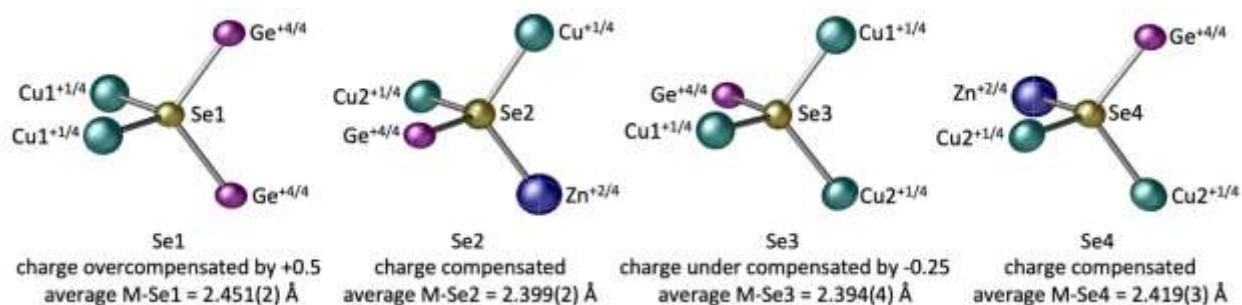


Figure 4. Each of the four crystallographically unique selenium atoms in the structure of  $\text{Cu}_4\text{ZnGe}_2\text{Se}_7$  with the average metal(M)-Se bond length provided. Se1 lies on a two-fold axis, while Se2, Se3 and Se4 reside on general positions. The individual electrostatic bond strengths are given next to each cation. The difference between the charge of selenium (-2) and the sum of the electrostatic bond strengths is equal to zero for the Se2 and Se4 atoms (i.e. local charge compensated).

Indeed, some subtle differences are noted in the metal-Se bonds in the  $\text{Cu}_4\text{ZnGe}_2\text{Se}_7$  structure. Se1 responds to its overcompensated-charge environment by lengthening the bonds with its cation neighbors. Se(1) has the longest average metal-Se distance in the structure. The Se1-Cu1 distances are the longest Cu-Se distances in the structure. Likewise, the Se1-Ge1 distances are  $\sim 0.08 \text{ \AA}$  longer than the next shortest Ge-Se bond distance. Because only a minor degree of charge undercompensation exists for the Se3 atom, a shortening of metal-Se3 bond distances is not observed. The average metal-Se3 bond distance is, within estimated standard deviations, identical to that of metal-Se2.

It should be noted that  $\text{Cu}^+$ ,  $\text{Zn}^{2+}$  and  $\text{Ge}^{4+}$  are isoelectronic and, consequently, nearly indistinguishable by X-ray diffraction due to their highly similar X-ray scattering cross sections. With this in mind, some other options were considered in the structure refinement. Switching Ge with either Cu1, Cu2 or Zn resulted in higher refinement statistics with  $R1/wR2$  values of 0.0536/0.1863, 0.0489/0.1639 and 0.0369/0.1216, respectively. Therefore, we are relatively confident in the position of the Ge atom. In fact, close examination of this site shows that it is rather unique, see Figure 5. While the average Ge-Se bond distance is similar to the Cu-Se and Zn-Se average, the Ge site clearly has the three shortest metal-Se bond distances. The one

longer Ge-Se bond is associated with the Se1 that serves as the bridge between germanium atoms in the  $[\text{Ge}_2\text{S}_7]^{6-}$  unit.

Cu/Zn disorder is common among related diamond-like materials, such as  $\text{Cu}_2\text{ZnSnS}_4$  (CZTS), and  $\text{Cu}_2\text{ZnSnSe}_4$  (CZTSe) [58,75-78]. However, the introduction of Cu/Zn disorder to the Cu1 site in  $\text{Cu}_4\text{ZnGe}_2\text{Se}_7$  resulted in an unstable refinement. On the other hand, the allowance Cu/Zn disorder on the Cu2 site resulted in similar R values to the current structural model reported here. Simultaneously permitting Cu/Zn disorder on both the Cu2 and Zn1 sites also resulted in similar refinement statistics. However, the chemical formula that resulted after the refinement of disorder on these two sites was unreasonable,  $\text{Cu}_{3.1}\text{Zn}_{1.9}\text{Ge}_2\text{Se}_7$ , as there is +14.9 charge from the cations and -14 charge from the anions. Therefore, considering the above refinement attempts, the EDS data and the ICP-OES results, we conclude that the current formula and structural model is the best one. Yet Cu/Zn disorder cannot be ruled out for the Cu2 and Zn1 sites. This is the limit of X-ray diffraction data; neutron diffraction would be more telling and is planned for the future because this requires a significantly large single crystal or relatively-large quantities of high-quality, microcrystalline powder on the order of several grams.

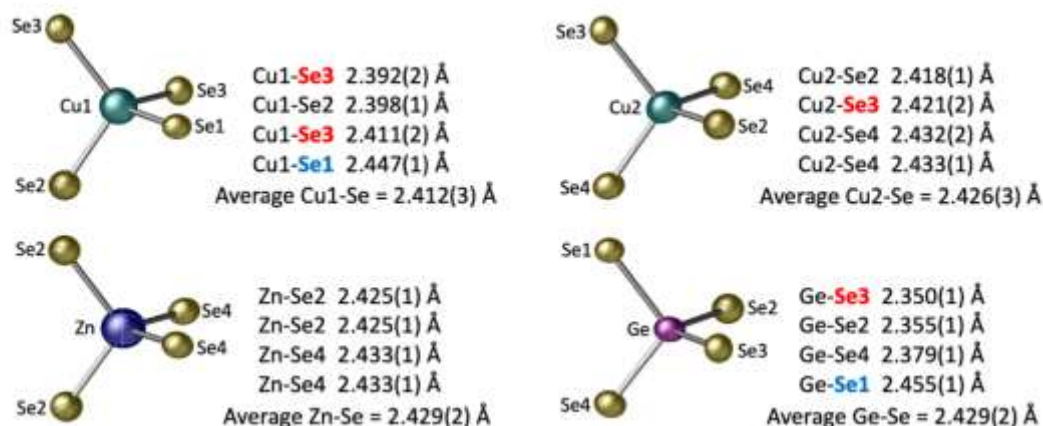


Figure 5. Each of the four crystallographic unique cations in the structure of  $\text{Cu}_4\text{ZnGe}_2\text{Se}_7$ . Zn lies on a two-fold axis, while Cu1, Cu2 and Ge are situated on general positions. The metal-selenium bond distances are provided for each tetrahedron. The Se3 atoms, shown in red, are undercompensated in terms of charge and are predicted by Pauling's second rule to participate in shorter bond distances. The charge of the Se1 atoms, displayed in blue, is overcompensated. Pauling's second rule predicts metal-Se1 bonds should be relatively long.

To further evaluate the structures, the bond valence sums (BVSs) and global instability index (G) were determined for  $\text{Cu}_4\text{ZnGe}_2\text{Se}_7$ , as well as  $\text{Cu}_2\text{ZnGeSe}_4$  in both reported structure types, Table 2. The BVS is the sum of the bond valences ( $s_{ij}$ ) around each ion in a compound, and is approximately equal to expected oxidation state of that ion. Each  $s_{ij}$  is calculated by using the experimentally determined bond distance,  $R_{ij}$ , and two constants,  $R_0$  and  $B$ , for a particular cation-anion pair, according to Equation 1 [79-83]. The BVS values were found to be similar and in reasonable agreement with the expected valencies of each ion in all cases, see Table 2. The G value for a compound, determined using Equation 2, represents the "plausibility" of a crystal structure and it gives a measure of how different the calculated BVS values are from the expected valencies ( $V_i$ ). A G value in the range of 0-0.05 reflects the expected experimental

uncertainties in the BVS values. Reasonable steric strain is indicated by a  $G$  value between 0.05 and 0.2. It is commonly accepted that, a  $G$  value greater than 0.2 indicates an unstable or possibly incorrect structure determination [80,84]. The  $G$  value for  $\text{Cu}_4\text{ZnGe}_2\text{Se}_7$ , as well as those calculated for stannite-type  $\text{Cu}_2\text{ZnGeSe}_4$  and kesterite type  $\text{Cu}_2\text{ZnGeSe}_4$ , were in the range that indicates stable structures with moderate levels of structural strain, Table 2.

$$\text{BVS} = \sum_j s_{ij}; s_{ij} = \exp[(R_0 - R_{ij})/b] \quad (1)$$

$$G = \sqrt{\frac{\sum_{i=1}^N (\text{BVS} - V_i)^2}{N}} \quad (2)$$

Table 2. Bond valence sums, provided for each crystallographically unique ion, and global instability index ( $G$ ) values for  $\text{Cu}_2\text{ZnGeSe}_4$  and  $\text{Cu}_4\text{ZnGe}_2\text{Se}_7$ .

Compound	Space Group	Bond Valence Sums*				G values	Structure Reference
		Cu <sup>+</sup>	Zn <sup>2+</sup>	Ge <sup>4+</sup>	Se <sup>2-</sup>		
$\text{Cu}_2\text{ZnGeSe}_4$	<i>I</i> -42 <i>m</i>	Cu (4e) 0.97	Zn (2d) 2.17	Ge(2b) 3.77	Se(8i) 1.97	0.10	[57]
$\text{Cu}_2\text{ZnGeSe}_4$	<i>I</i> -4	Cu1(2a) 0.91 Cu2(2c) 1.00	Zn(2d) 2.17	Ge(2b) 3.87	Se(8g) 1.99	0.08	[58]
$\text{Cu}_4\text{ZnGe}_2\text{Se}_7$	<i>C</i> 2	Cu1(4c) 1.00 Cu2(4c) 0.97	Zn(2a) 2.27	Ge(4c) 3.66	Se1(2b) 1.96 Se2(4c) 2.07 Se3(4c) 1.76 Se4(4c) 1.96	0.18	this work

\* $R_0$  values for the specified oxidation states were used in all cases. Note that the  $R_0$  value for  $\text{Ge}^{4+}$ - $\text{Se}^{2-}$  bond is listed as "unchecked"[83].

### 3.2 Synchrotron X-ray powder diffraction and Rietveld refinements

Analysis of laboratory X-ray powder diffraction data obtained for  $\text{Cu}_2\text{ZnGeSe}_4$  and  $\text{Cu}_4\text{ZnGe}_2\text{Se}_7$  samples was hindered by the fact that the X-ray powder diffraction patterns have many similar overlapping, or near overlapping, peaks as both compounds are DLSs with structures derived from cubic diamond. To further complicate matters, the two compounds contain isoelectronic ions,  $\text{Cu}^+$ ,  $\text{Zn}^{2+}$  and  $\text{Ge}^{4+}$ , that are nearly indistinguishable by X-ray diffraction. Therefore, high-resolution, synchrotron X-ray powder diffraction data were collected for both samples at beamline 11-BM at the Advanced Photon Source of Argonne National Laboratory.

For the  $\text{Cu}_2\text{ZnGeSe}_4$  sample, all of the reflections in the powder diffraction pattern could be indexed to either the stannite-type or kesterite-type structure; no other reflections were present, indicating that  $\text{Cu}_2\text{ZnGeSe}_4$  was prepared in phase-pure form. Reflections belonging to  $\text{Cu}_4\text{ZnGe}_2\text{Se}_7$  were specifically looked for and no evidence was observed for any  $\text{Cu}_4\text{ZnGe}_2\text{Se}_7$  in the  $\text{Cu}_2\text{ZnGeSe}_4$  sample. Unfortunately, we could not distinguish between the stannite and kesterite structure types for  $\text{Cu}_2\text{ZnGeSe}_4$ ; adequate and similar refinement statistics were obtained in either case. Based on the fact that the neutron scattering cross sections of the cations in question are sufficiently different, we have a higher level of confidence in the

kesterite-type structure put forward by Schorr and team [58]; therefore, the refinement of  $\text{Cu}_2\text{ZnGeSe}_4$  with the kesterite structure using our data, is presented in Figure 6 left. It should be noted that one cannot rule out the existence of polymorphs for  $\text{Cu}_2\text{ZnGeSe}_4$  and we are not implying that the stannite structure is incorrect, as diamond-like materials are notorious for crystallizing in different structures, e.g. there are  $\sim 200$  polymorphs of ZnS [85,86]. Furthermore, even slightly different preparation conditions may account for the presence of polymorphs.

In the case of the  $\text{Cu}_4\text{ZnGe}_2\text{Se}_7$  sample, the majority of the reflections in the powder diffraction pattern could be indexed to the intended phase; however, the high-resolution, synchrotron data clearly showed additional small peaks that were not distinguishable in the laboratory X-ray powder diffraction of the same sample, due to the overlap of peaks inherent in the laboratory X-ray powder diffraction measurement. These extra peaks could be indexed to  $\text{Cu}_2\text{ZnGeSe}_4$  (stannite or kesterite type) and, therefore, the refinement for the  $\text{Cu}_4\text{ZnGe}_2\text{Se}_7$  sample was carried out using a two-phase model of  $\text{Cu}_4\text{ZnGe}_2\text{Se}_7$  and the kesterite-type  $\text{Cu}_2\text{ZnGeSe}_4$ , Figure 6 right. The final Rietveld refinement resulted in  $\sim 70.6$  and  $\sim 29.4$  wt% for  $\text{Cu}_4\text{ZnGe}_2\text{Se}_7$  and  $\text{Cu}_2\text{ZnGeSe}_4$ , respectively.

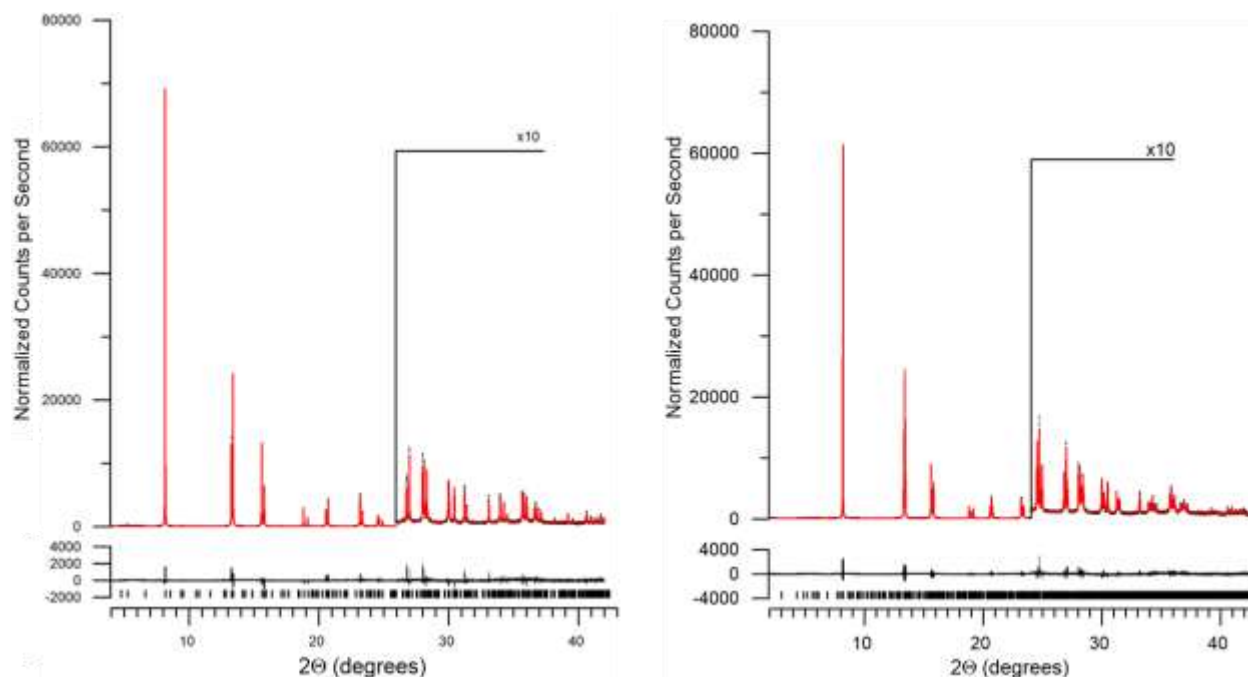


Figure 6. The results of Rietveld refinements for  $\text{Cu}_2\text{ZnGeSe}_4$  (left) and  $\text{Cu}_4\text{ZnGe}_2\text{Se}_7$  (right) samples using high-resolution synchrotron X-ray powder diffraction patterns collected with 27 keV X-rays,  $\lambda = 0.4590 \text{ \AA}$ . The collected data are drawn using a black dotted line, the pattern calculated from the model is traced in red, and the difference between these two is given in black below on the same scale. Expected Bragg reflections for the primary phase are indicated with tic marks (|).

### 3.3 Synthesis, Morphology and Composition

$\text{Cu}_2\text{ZnGeSe}_4$  could be prepared as a single phase but this result took many trials. Reactions were carried out with the highest temperature ranging from 700 to 850 °C and hold-times spanning two days to two weeks. Both  $\text{Cu}_2\text{GeSe}_3$  [87] and  $\text{ZnSe}$  were frequently encountered as secondary phases, in addition to  $\text{Cu}_2\text{ZnGeSe}_4$ . It should be noted that the success of the reaction was also sensitive to other conditions besides temperature and time. Using the conditions given in the experimental section and additionally grinding the reactants before placing them into the fused-silica tube clearly resulted in noticeable secondary phases. Additionally, halving the reaction also resulted in secondary phases. This leads one to believe that proper stoichiometry is important to achieving a pure sample, as halving a reaction magnifies weighing errors and the grinding of reactants may preferentially leave some reactants stuck to the mortar and pestle. As selenium is the most volatile of the elemental reactants, it seems logical that a 5% excess of selenium was needed to achieve the best results presented in Figure 6 left. Additionally, an excess of selenium has also been used by other researchers to achieve phase-pure  $\text{Cu}_2\text{ZnGeSe}_4$  [69,71].

Unfortunately, a phase-pure sample of  $\text{Cu}_4\text{ZnGe}_2\text{Se}_7$  could not be achieved, despite many trials. Using only stoichiometric amounts of selenium in attempt to prepare  $\text{Cu}_4\text{ZnGe}_2\text{Se}_7$  resulted in increased secondary phase formation. Because the sample of  $\text{Cu}_4\text{ZnGe}_2\text{Se}_7$  appeared phase pure using laboratory-grade XRPD and the minor amount of the  $\text{Cu}_2\text{ZnGeSe}_4$  secondary phase could only be detected using synchrotron data, it was determined that the sample would be acceptable for further characterization.

Interestingly, the  $\text{Cu}_4\text{ZnGe}_2\text{Se}_7$  phase was not observed during the  $\text{Cu}_2\text{GeSe}_3$ - $\text{ZnSe}$  phase diagram study conducted by Parasyuk *et al.* [57], although the  $\text{Cu}_4\text{ZnGe}_2\text{Se}_7$  phase corresponds to 33.33 mole %  $\text{ZnSe}$ . A 70/30 mole%  $\text{Cu}_2\text{GeSe}_3$ - $\text{ZnSe}$  sample was investigated in Parasyuk's study; however, the elemental reagents were heated to 1270 K (~1000 °C), which is considerably higher than our synthesis temperature of 800 °C. Additionally, Parasyuk and coworkers annealed the samples for nearly 21 days. As both increased temperature and time resulted in less of the  $\text{Cu}_4\text{ZnGe}_2\text{Se}_7$  phase and more of the  $\text{Cu}_2\text{ZnGeSe}_4$  in our reactions, it is, perhaps, not surprising that the  $\text{Cu}_4\text{ZnGe}_2\text{Se}_7$  phase was not discovered in Parasyuk's investigation. Additionally, a small amount of  $\text{Cu}_4\text{ZnGe}_2\text{Se}_7$  could be difficult to detect in the samples due to the striking similarity between the  $\text{Cu}_4\text{ZnGe}_2\text{Se}_7$  X-ray powder diffraction pattern and that of  $\text{Cu}_2\text{ZnGeSe}_4$  (either the kesterite and stannite type).

The visually similar samples of  $\text{Cu}_2\text{ZnGeSe}_4$  and  $\text{Cu}_4\text{ZnGe}_2\text{Se}_7$  contained dark, grayish-black polyhedral crystals of various shapes, including rods, Figure 7. The crystals varied in size between 10  $\mu\text{m}$  to 200  $\mu\text{m}$  on an edge. Semi-quantitative elemental analysis using EDS gave an average formulae of  $\text{Cu}_{2.1(1)}\text{Zn}_{1.0(1)}\text{Ge}_{1.1(1)}\text{Se}_{4.2(3)}$  and  $\text{Cu}_{4.1(2)}\text{Zn}_{1.0(1)}\text{Ge}_{2.1(1)}\text{Se}_{7.1(3)}$  for  $\text{Cu}_2\text{ZnGeSe}_4$  and  $\text{Cu}_4\text{ZnGe}_2\text{Se}_7$ , respectively, in relatively close agreement with the expected results. To

further corroborate the compositional results, quantitative ICP-OES was also performed, giving the formulae of  $\text{Cu}_{2.0(2)}\text{Zn}_{1.0(1)}\text{Ge}_{1.1(1)}\text{Se}_{3.9(4)}$  and  $\text{Cu}_{3.9(4)}\text{Zn}_{1.0(1)}\text{Ge}_{2.2(2)}\text{Se}_{6.8(7)}$ .

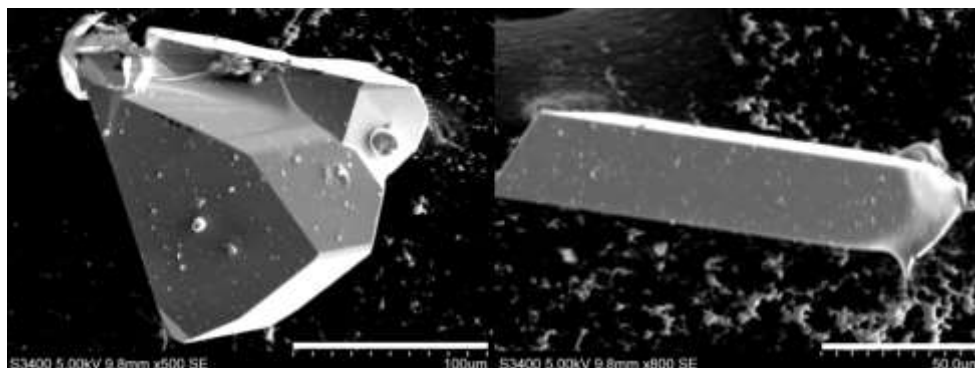


Figure 7. Representative secondary electron images of  $\text{Cu}_4\text{ZnGe}_2\text{Se}_7$  crystals. The white scale bar drawn in the bottom right corner of each micrograph corresponds to 100  $\mu\text{m}$  (left) and 50  $\mu\text{m}$  (right).

### 3.4 Thermal analysis.

In 2000, Matsushita *et al.* reported that  $\text{Cu}_2\text{ZnGeSe}_4$  melts congruently at 1163 K ( $\sim 890^\circ\text{C}$ ); however, the DTA diagram was not provided in that publication and the authors did not explain how the congruency of melting was determined [70]. Parasyuk *et al.* [57] observed a more complex thermogram indicative of incongruent melting. They reported that  $\text{Cu}_2\text{ZnGeSe}_4$  undergoes a polymorphous transformation at 1071 K ( $\sim 798^\circ\text{C}$ ) and a peritectic decomposition at 1168 K ( $\sim 895^\circ\text{C}$ ). They also noted an additional exothermic event at higher temperature in the cooling curves that was assigned to the crystallization of ZnSe (liquidus). Unfortunately, the temperature for this event was not provided and the thermograms in the manuscript did not display a temperature axis.

The complete DTA diagram for  $\text{Cu}_2\text{ZnGeSe}_4$  is displayed in Figure 8. In the first cycle, one endothermic event is clearly visible at  $868^\circ\text{C}$  upon heating and one obvious exothermic event is apparent at  $885^\circ\text{C}$  upon cooling. A second event in the cooling curve at  $\sim 788^\circ\text{C}$  is barely visible. In the second cycle, one obvious endothermic event is evident at  $881^\circ\text{C}$  and an additional, barely visible event seems to appear at  $788^\circ\text{C}$ . Upon cooling, two exotherms are apparent at  $885^\circ\text{C}$  and  $796^\circ\text{C}$ . These results are similar to those that were observed by Parasyuk and coworkers [57]. We did not, however, observe any events higher than  $885^\circ\text{C}$ . Because the two cycles of DTA are nearly identical this suggests that the events are reversible.

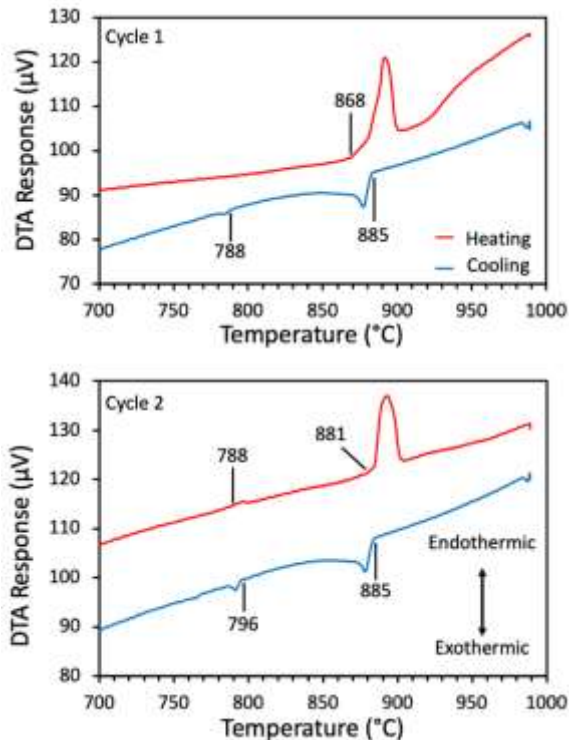


Figure 8. Differential thermal analysis diagrams for  $\text{Cu}_2\text{ZnGeSe}_4$ . The two plots above represent the heating (red) and cooling (blue) curves for cycle 1 (top) and cycle 2 (bottom) of the same experiment.

The DTA diagram obtained for a  $\text{Cu}_4\text{ZnGe}_2\text{Se}_7$  sample is plotted in Figure 9. Upon heating in the first cycle of the experiment, three endothermic events are observed: one barely noticeable event at 753 °C and a two closely spaced events at 876 °C and 882 °C. Upon cooling, two exothermic events are observed, two obvious peaks at 879 and 781 °C. In the second cycle, two endothermic events are noted at 762 and 877 °C and two exothermic events are recorded at 878 and 781 °C. It is interesting to note that just as in the case of  $\text{Cu}_2\text{ZnGeSe}_4$ , we did not observe any transitions higher than 885 °C for  $\text{Cu}_4\text{ZnGe}_2\text{Se}_7$ .

It should be noted that the DTA diagrams for  $\text{Cu}_2\text{ZnGeSe}_4$  and  $\text{Cu}_4\text{ZnGe}_2\text{Se}_7$  are very similar with the events for  $\text{Cu}_4\text{ZnGe}_2\text{Se}_7$  occurring at slightly lower temperatures. In the study by Matsushita et al., it was found that the melting point temperature of quaternary diamond-like materials decreased linearly with increasing mean atomic weight. By digitizing the data in the Matsushita paper, the slope could be calculated as  $\sim 9 \text{ }^\circ\text{C g}^{-1} \text{ mol}^{-1}$ . For  $\text{Cu}_2\text{ZnGeSe}_4$  and the  $\text{Cu}_4\text{ZnGe}_2\text{Se}_7$  only a small difference in the temperatures of the thermal events is expected because the title compounds mean atomic weights vary only slightly, 72.62 and 72.69 g/mol, respectively.

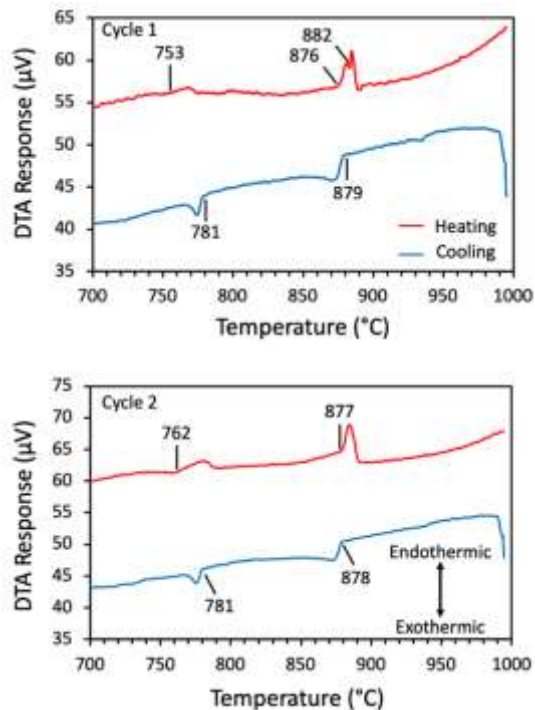


Figure 9. Differential thermal analysis diagrams for  $\text{Cu}_4\text{ZnGe}_2\text{Se}_7$ . The two plots above represent the heating (red) and cooling (blue) curves for cycle 1 (top) and cycle 2 (bottom) of the same experiment.

It seems reasonable to propose an incongruent melting behavior for  $\text{Cu}_4\text{ZnGe}_2\text{Se}_7$ , similar to that which was proposed by Parasyuk et al. [57] for  $\text{Cu}_2\text{ZnGeSe}_4$ , see Table S8. Upon heating,  $\text{Cu}_4\text{ZnGe}_2\text{Se}_7$  undergoes a solid-solid phase transition, next the high-temperature phase undergoes a peritectic decomposition to  $\text{Cu}_2\text{GeSe}_3$  liquid and ZnSe solid. Although we do not observe a peak in the thermogram for ZnSe melting into the  $\text{Cu}_2\text{GeSe}_3$  liquid, this event cannot be ruled out, as the occurrence of melting may not be a rapid event, but rather a prolonged process occurring over a relatively broad temperature range. It should be noted that solid-solid phase transitions are common among diamond-like materials. Upon cooling, the crystallization of ZnSe (liquidus) may occur followed by the peritectic formation of the high-temperature form of  $\text{Cu}_4\text{ZnGe}_2\text{Se}_7$  and finally  $\text{Cu}_4\text{ZnGe}_2\text{Se}_7$  transforms to the C2 structure. In light of the novel  $\text{Cu}_4\text{ZnGe}_2\text{Se}_7$  compound reported here, the DTA data and the data available from the literature, we propose a new  $(\text{Cu}_2\text{GeSe}_3)_{1-x}(\text{ZnSe})_x$  phase diagram, see Figure 10. While this diagram is an improvement from that previously presented [57], we speculate that the temperature-x phase diagram for the  $(\text{Cu}_2\text{GeSe}_3)_{1-x}(\text{ZnSe})_x$  system may be even more complicated than that presented here. There are several hypothetical compounds that, if stable, should possess structures derived from diamond. These materials are predicted using two valence electron rules: 1) the average number of valence electrons must equal four, and 2) the number of valence electrons per anion must equal eight. As a consequence, the number of cations must equal the number of anions in the formula. Further work in this system to target these possible compositions, such as  $\text{Cu}_6\text{ZnGe}_3\text{Se}_{10}$  (where  $x=1/4$ ) or  $\text{Cu}_2\text{Zn}_2\text{GeSe}_5$  (where  $x=2/3$ ) may provide additional information.

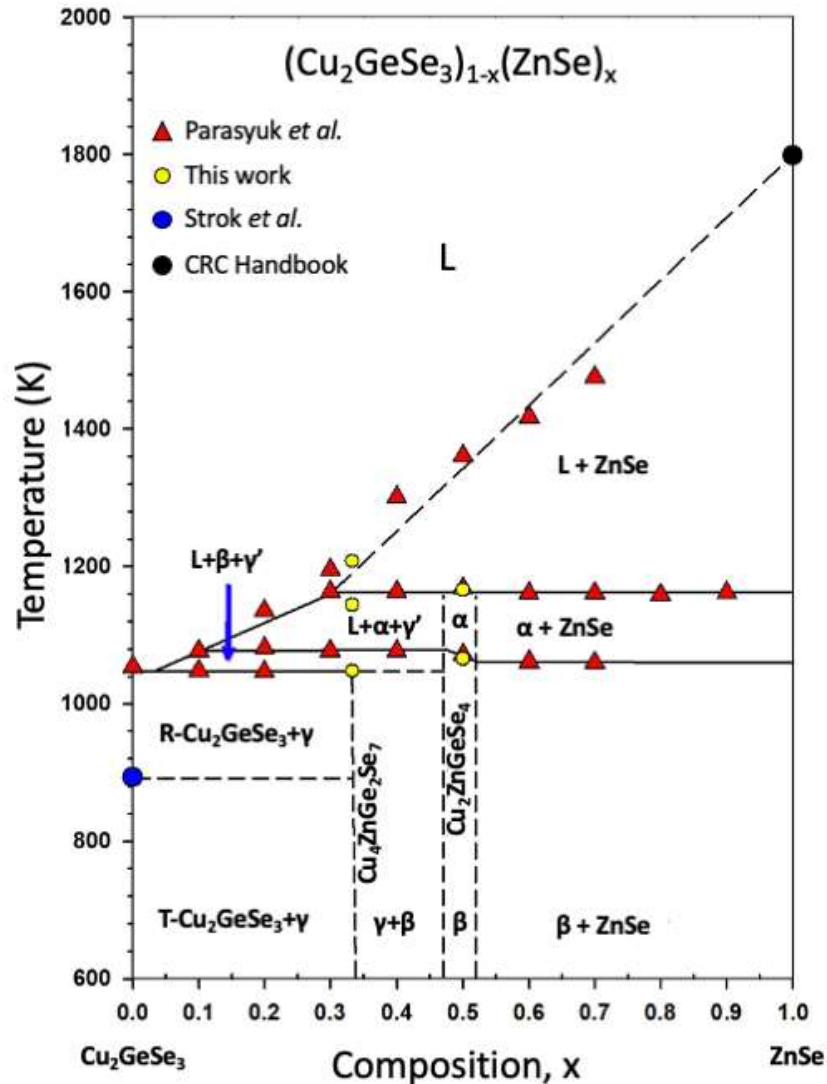


Figure 10. A new, proposed phase diagram for  $(\text{Cu}_2\text{GeSe}_3)_{1-x}(\text{ZnSe})_x$  based on the data presented here as well as that reported by Parasyuk et al. [57], Stok et al. [88], and Kulakov et al. [89]. The rhombohedral (R) and tetragonal (T) phases of  $\text{Cu}_2\text{GeSe}_3$  crystallize in space groups  $Imm2$  (No. 44) and  $I-42d$  (No. 122) respectively [90,91]. The vertical dashed line, from the blue circle to the vertical dashed line at  $x=1/3$  is only speculative.

### 3.5 Optical Bandgaps

Optical diffuse reflectance spectra converted to absorption for powdered samples of  $\text{Cu}_2\text{ZnGeSe}_4$  and  $\text{Cu}_4\text{ZnGe}_2\text{Se}_7$  are displayed in Figure 11. Before estimating the optical bandgaps of semiconductors, the Urbach tail regions should be identified because it permits the homogeneity of the sample to be gauged and gives the lower limit for the bandgap energy [92]. The Urbach tail near the optical absorption edge generally arises from defects and disorder in semiconductors that manifests itself in a “smearing” of the density of states near the valence band maximum and conduction band minimum [93,94]. In order to pinpoint the Urbach tail region of each spectrum, the logarithm (log) of the absorption versus photon energy was plotted and the linear region of the curve was fit using the equation  $\alpha = A \cdot \exp[(E-E_g)/E_u]$ ,

where  $A$  is a constant,  $E$  is the photon energy,  $E_g$  is the bandgap energy and  $E_u$  is the Urbach energy. Once the Urbach tail regions were recognized, they were excluded from the bandgap determinations.

Sharp optical absorption edges are observed for direct bandgap semiconductors, whereas indirect bandgap semiconductors generally display a more gradual onset of absorption [93]. Data at energies higher than the Urbach tail region were fit to the functions for a direct and an indirect bandgap semiconductor. For both compounds a wider linear region was distinguishable when the data were plotted as  $(\alpha E)^2$  versus  $E$ , as opposed to  $(\alpha E)^{1/2}$  vs.  $E$ , indicating that the bandgaps are direct in nature. Extrapolation of this linear region of the absorption edge to the x-axis gave bandgap values of 1.38 and 0.91 eV for  $\text{Cu}_2\text{ZnGeSe}_4$  and  $\text{Cu}_4\text{ZnGe}_2\text{Se}_7$ , corresponding to  $\sim 900$  and  $1364$  nm, respectively.

The bandgap of  $\text{Cu}_2\text{ZnGeSe}_4$  has been measured by several research groups in the past. Our bandgap value agrees relatively well with that obtained by Schleich and Wold, 1.29 eV, for crystals prepared by iodine vapor transport [68]. The value obtained by Lee and Kim for crystals grown by  $\text{I}_2$ -transport is somewhat larger at 1.518 eV (direct) and they propose that the discrepancy between the bandgap that they obtained and that obtained by Schleich and Wold is likely due to crystal quality, more specifically we believe that they are referring to stoichiometry [69]. Matsushita et al. reported a value of 1.63 eV obtained for crystals grown by the horizontal gradient freeze method [70]. Furthermore, values of 1.49 and 1.63 eV (direct) have been reported for  $\text{Cu}_2\text{ZnGeSe}_4$  thin films [71,95].

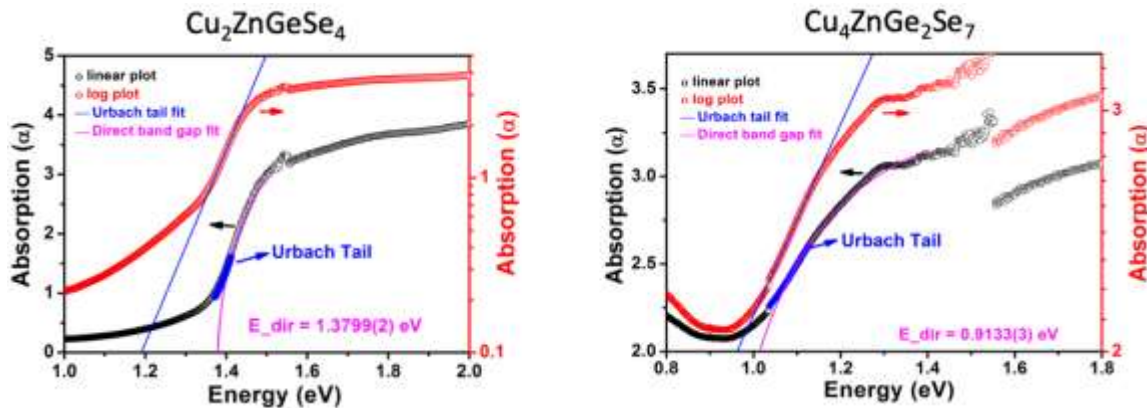


Figure 11. Optical diffuse reflectance data converted to absorption using the Kubelka-Munk function is plotted against the left-hand y-axes for  $\text{Cu}_2\text{ZnGeSe}_4$  (left) and  $\text{Cu}_4\text{ZnGe}_2\text{Se}_7$  (right). The log of the absorption data is displayed on the right-hand y-axes. The discontinuity around 1.55 eV is due to a detector change.

### 3.6 Electronic Structure

In order to investigate the origin of the bandgap, electronic structure calculations were carried out using density functional theory (DFT) within the CASTEP code. Figure 11 displays the electronic band structure, total DOS and pDOS for  $\text{Cu}_4\text{ZnGe}_2\text{Se}_7$ . Since  $\text{Cu}_2\text{ZnGeSe}_4$  is a promising solar cell absorber material, electronic structure calculations have previously been reported by several research groups [49-52]. The electronic structure of  $\text{Cu}_4\text{ZnGe}_2\text{Se}_7$ , which is

presented here for the first time, will be described in detail and compared to that of  $\text{Cu}_2\text{ZnGeSe}_4$ .

In the electronic band structure of  $\text{Cu}_4\text{ZnGe}_2\text{Se}_7$  a direct bandgap occurs at the  $\Gamma$  point with a value of 0.62 eV, see Figure 12. This value is underestimated due to the limitations of DFT methods. Likewise, previous electronic structure calculations for kesterite-type  $\text{Cu}_2\text{ZnGeSe}_4$  have also resulted in underestimated bandgaps [49-52]. The states at the valence band maximum,  $\text{VB}_{\text{Max}}$ , for  $\text{Cu}_4\text{ZnGe}_2\text{Se}_7$  possess mainly copper  $d$  and selenium  $p$  character, which is a common feature of ternary and quaternary copper-containing diamond-like chalcogenides. These states have been attributed to an antibonding interaction between copper and the chalcogen. There is very little involvement from the germanium  $p$  orbitals to the states at the  $\text{VB}_{\text{Max}}$ . The atomic orbitals of zinc chiefly donate to the states in the valence band below -5 eV. The conduction band minimum,  $\text{CB}_{\text{Min}}$ , is majorly influenced by the  $[\text{Ge}_2\text{Se}_7]^{6-}$  units, with the Ge  $s$ , Se  $s$  and Se  $p$  orbitals providing the greatest contributions to those states. The germanium  $p$  orbitals play a significant role in the conduction band between 2 and 5 eV. Higher in the conduction band, the copper  $s$  and  $p$  orbitals notably impact the states above 5 eV.

Chen and Ravindra calculated the electronic structure of  $\text{Cu}_2\text{ZnGeSe}_4$  in both the stannite and kesterite structures [50]. They noted a great likeness between the results and plotted only the data for the kesterite structure, as it was determined to be the lower energy phase. The general shape of the DOS calculated by Chen and Ravindra for  $\text{Cu}_2\text{ZnGeSe}_4$  is strikingly similar to that shown in Figure 11 for  $\text{Cu}_4\text{ZnGe}_2\text{Se}_7$ , see supporting information Figure S1.

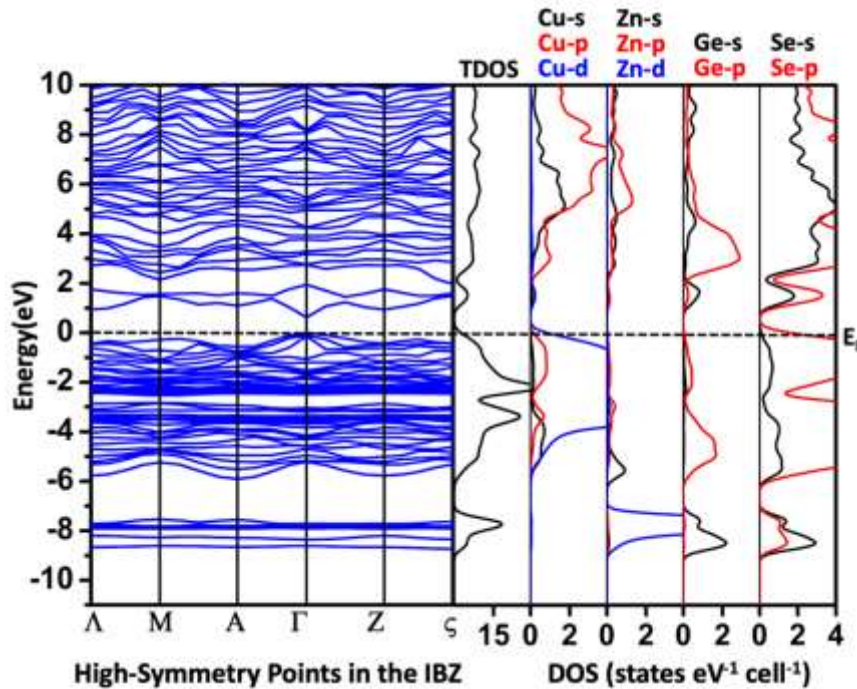


Figure 12. Electronic band structure, total density of states (DOS) and partial DOS displayed from left to right for  $\text{Cu}_4\text{ZnGe}_2\text{Se}_7$ .

### 3.7 Transparency

Both title compounds were analyzed using attenuated total reflectance (ATR) FT-IR spectroscopy. The ATR data were transformed to percent transmittance and stitched together with the diffuse reflectance UV/Vis/NIR data that was also converted to percent transmittance, Figure 13.  $\text{Cu}_2\text{ZnGeSe}_4$  demonstrates a potentially wide window of optical clarity; beyond its bandgap, 0.9  $\mu\text{m}$  (1.38 eV),  $\text{Cu}_2\text{ZnGeSe}_4$  is >70% transparent.  $\text{Cu}_4\text{ZnGe}_2\text{Se}_7$  shows some absorption even past the band edge  $\sim 1.4 \mu\text{m}$  (0.91 eV), but still displays high transparency, >80%, from 3-25  $\mu\text{m}$ . Although the limit of our instrumentation is 25  $\mu\text{m}$ , the transparency of the title compounds likely extends well into the far-IR. While oxide materials tend to absorb in the infrared and are, therefore, better suited for visible and UV NLO applications, these selenides are prime candidates for IR NLO devices due to their wide transparency range in the infrared, including the two major atmospheric transparency windows.

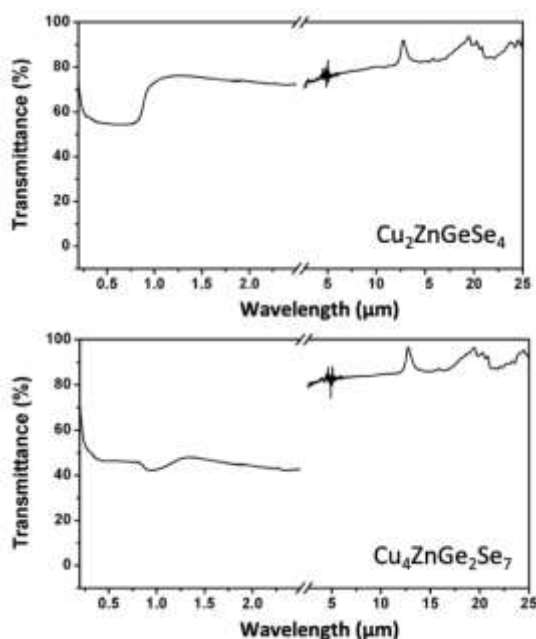


Figure 13. Transmittance (%) for  $\text{Cu}_2\text{ZnGeSe}_4$  (top) and  $\text{Cu}_4\text{ZnGe}_2\text{Se}_7$  (bottom). These plots were created by stitching together the diffuse reflectance UV/Vis/NIR spectra (0.2-2.5  $\mu\text{m}$ ) and the attenuated total reflectance FT-IR spectra (2.5-25  $\mu\text{m}$ ), both converted to transmittance.

### 3.8 Second Harmonic Generation

Second-order nonlinear optical susceptibility,  $\chi^{(2)}$ , is the lowest-order optical nonlinearity of a noncentrosymmetric material. Generally, rotational and/or the Maker fringes method [96,97] are employed to determine the  $\chi^{(2)}$  of a material; however, these techniques are only viable for thin film and single crystal samples. Here we present SHG responses from powdered samples by employing the Kurtz-Perry powder technique [62] when  $\lambda$  is tuned over a broad range.

Firstly, the SHG response was measured for an optical-quality reference material, AGSe. Figure 14a displays the broadband SHG response from AGSe for  $d$  in the range of 20-45  $\mu\text{m}$ , when the incident  $\lambda$  was tuned from 2900 to 3900 nm. Within our excitation intensity, multiphoton

absorption (MPA) was negligible in this region. The  $\lambda$ -dependent SHG response indicates a constant stagnant regime [98]. Figure 14b provides the particle size dependence of the SHG at  $\lambda=2900$  nm. The experimental PM trend is rather unclear; however, AGSe at this wavelength is not PM with a long coherence length of  $\sim 120$   $\mu\text{m}$ . Such a long coherence length indeed indicates a boundary between PM and non-PM, where the PM onset of AGSe is 3100 nm [99]. We determined the NLO coefficient of  $\text{Cu}_2\text{ZnGeSe}_4$  at  $\lambda=2900$  nm, where both the sample and the reference are non-PM with limited MPA influence. The absolute value of the second order NLO coefficient of the sample,  $\chi_S^{(2)}$ , is determined based on exact comparison with the reference value of AGSe,  $\chi_R^{(2)} = 66$  pm/V for non-PM case [98];

$$\chi_S^{(2)} = \chi_R^{(2)} \left| \frac{I_S(2\omega)}{I_R(2\omega)} \right|^{1/2} \frac{l_R}{l_S}, \quad (3)$$

where  $I_S(2\omega)$  and  $I_R(2\omega)$  correspond to SHG counts from the sample and the reference, respectively, and  $l_S$  and  $l_R$  are the corresponding SHG coherence lengths of the sample and the reference, respectively. Here  $l_S=32$   $\mu\text{m}$  was experimental determined by the average particle size corresponding to the maximum SHG response in Figure 15a, whereas  $l_R$  was computed from  $l_R = \frac{\lambda}{4[n_{2\omega} - n_\omega]} \sim 120$   $\mu\text{m}$ , where  $n_{2\omega} = \sqrt{3.3132 + \frac{3.3616\lambda^2}{\lambda^2 - (0.38201)^2} + \frac{1.7677\lambda^2}{\lambda^2 - 1600}} \sim 2.631$  at  $\lambda = 1.45$   $\mu\text{m}$  and  $n_\omega = \sqrt{3.9362 + \frac{2.9113\lambda^2}{\lambda^2 - (0.38821)^2} + \frac{1.7954\lambda^2}{\lambda^2 - 1600}} \sim 2.625$  at  $\lambda = 2.9$   $\mu\text{m}$  are refractive indices at SHG and fundamental wavelengths, respectively [99]. Here  $n_{2\omega}$  and  $n_\omega$  correspond to extraordinary and ordinary refractive indices since AGSe is a negative uniaxial crystal and  $\lambda$  is given in microns [99].

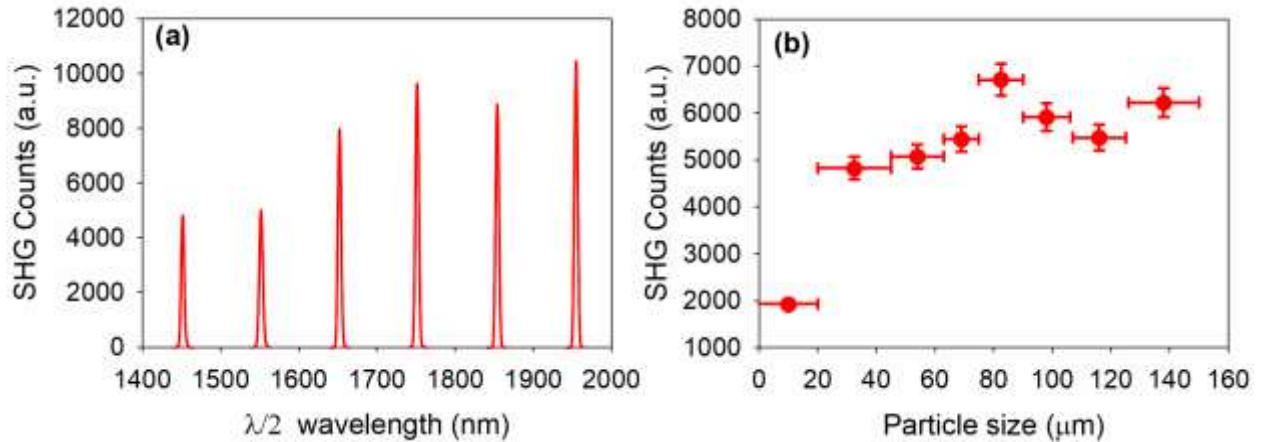


Figure 14. (a) Broadband SHG response of the AGSe reference, plotted in terms of SHG wavelength (incident  $\lambda = 2900 - 3900$  nm). (b) Particle size dependence of SHG for AGSe at  $\lambda = 2900$  nm, which is near the boundary between PM and non-PM for the reference.

In Figure 15a, the SHG counts as a function of particle size for  $\text{Cu}_2\text{ZnGeSe}_4$  are shown for  $\lambda = 2900$  nm. The decrease in SHG counts with an increase in particle size demonstrates that the material is non-PM at this wavelength. In fact,  $\text{Cu}_2\text{ZnGeSe}_4$  was not phase matchable within our observation range, Figure S2. The blue dots in Figure 15b correspond to the wavelength-dependent SHG counts for  $\text{Cu}_2\text{ZnGeSe}_4$  with  $d=20-45$   $\mu\text{m}$  plotted on a semi-log scale. The

wavelength-dependent SHG counts from AGSe of the same particle size are plotted as red dots for direct comparison. A leveling trend of the SHG counts with increasing  $\lambda$  indicates that the SHG response of  $\text{Cu}_2\text{ZnGeSe}_4$  is also static within the observation range. Using Eq(3) yields that the  $\chi^{(2)}$  for  $\text{Cu}_2\text{ZnGeSe}_4$  is  $\sim 43 \pm 6$  pm/V at  $\lambda = 2900$  nm.

The SHG response of  $\text{Cu}_4\text{ZnGe}_2\text{Se}_7$  is significantly small as compared to AGSe and  $\text{Cu}_2\text{ZnGeSe}_4$  and was only measurable at two wavelengths, 2900 and 3100 nm, Figure S3. For example, for  $d=20\text{-}45$   $\mu\text{m}$ , the SHG efficiency of  $\text{Cu}_4\text{ZnGe}_2\text{Se}_7$  is 980 and 1120 times weaker than that of AGSe at 2900 and 3100 nm, respectively. The larger sized particles,  $d > 100$   $\mu\text{m}$ , produced nearly no signal. The nominal SHG response of  $\text{Cu}_4\text{ZnGe}_2\text{Se}_7$  could be attributed to absorption effects of both the fundamental and SHG light (see Figure 13 bottom), coupled together with the large Urbach tailing effects (see Figure 11 right).

Second-order NLO properties are utilized in NLO devices in frequency doubling/SHG and difference frequency generation (DFG). As a result, a noncentrosymmetric material with a large  $\chi^{(2)}$  like that of  $\text{Cu}_2\text{ZnGeSe}_4$  would be excellent for second-order NLO applications. Yet the relatively narrow bandgaps of  $\text{Cu}_2\text{ZnGeSe}_4$  and  $\text{Cu}_4\text{ZnGe}_2\text{Se}_7$  render them susceptible to two-photon absorption within the framework of the Nd:YAG laser line ( $\lambda = 1064$  nm) that compromises their LIDT and, therefore, limits practical applications for high-power NLO devices. However,  $\text{Cu}_2\text{ZnGeSe}_4$  could still be viable for low-power NLO applications.

The  $\chi^{(2)}$  of  $\text{Cu}_2\text{ZnGeSe}_4$  is significantly higher than several of the benchmark NLO materials and other DLSs that we have measured previously [14,35,29]. For example,  $\text{AgGaSe}_2$  with a bandgap of 2.62 eV [10] has a  $\chi^{(2)}$  value of only 36 pm/V [6]. Furthermore, it should be noted that because the “homemade” microcrystalline samples prepared in this study were assessed using an optical-quality AGSe reference, the  $\chi^{(2)}$  value may be underestimated and can be considered as a lower bound on the  $\chi^{(2)}$ . In fact, our “homemade” microcrystalline sample of AGSe gives an SHG response less than half that of the optical quality sample [35]. Therefore, it is quite possible that  $\text{Cu}_2\text{ZnGeSe}_4$  could have a higher  $\chi^{(2)}$ , perhaps even greater than AGSe (66 pm/V [99]), if it could be prepared as a commercial-grade, optical-quality single crystal.

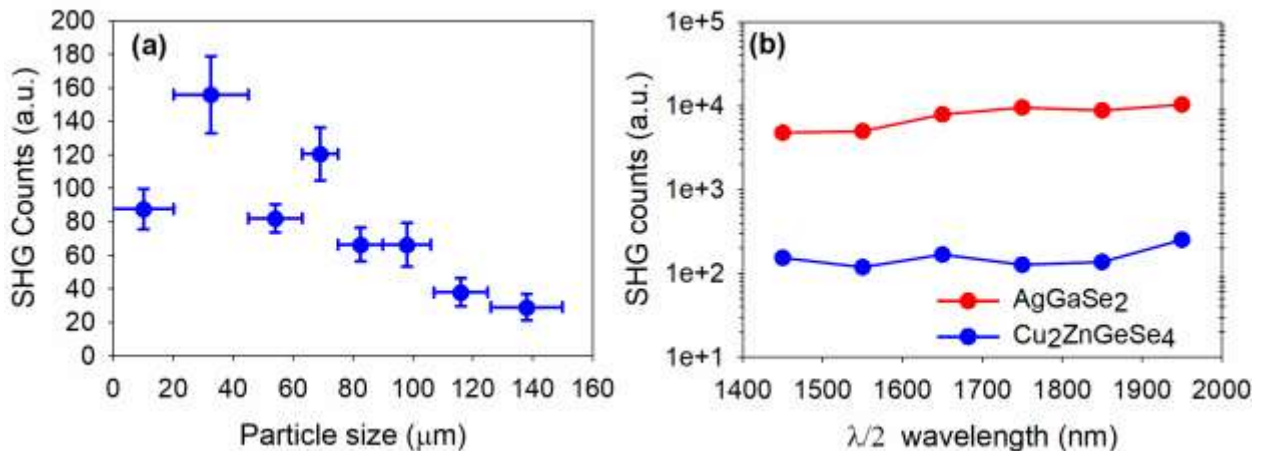


Figure 15. (a) Particle size dependence of SHG for  $\text{Cu}_2\text{ZnGeSe}_4$ , indicating a non-PM case at  $\lambda = 2900$  nm. (b) Relative SHG efficiencies of  $\text{Cu}_2\text{ZnGeSe}_4$  (blue) and  $\text{AGSe}$  (red) as a function of SHG wavelength (incident  $\lambda = 2900 - 3900$  nm).

#### 4. Conclusion

The known  $\text{Cu}_2\text{ZnGeSe}_4$  and the new  $\text{Cu}_4\text{ZnGe}_2\text{Se}_7$  differ in terms of their stoichiometry and their space group symmetry, but they are both DLSs with crystal structures that can be considered as derivatives of cubic diamond. Additionally, they both possess wide windows of optical clarity in the infrared, relatively high thermal stability, and SHG responses. Moreover, the electronic structures are also very similar with the states near the  $E_F$  being dominated by contributions from the Cu  $d$  orbitals and Se  $p$  orbitals at the valence band maximum and conduction band minimum, respectively, a hallmark of copper-containing DLS chalcogenides. However, the SHG responses of the two materials are significantly different;  $\text{Cu}_4\text{ZnGe}_2\text{Se}_7$  displays a weak SHG response, while  $\text{Cu}_2\text{ZnGeSe}_4$  gives rise to the strongest SHG response that our group has measured for a quaternary DLS. While the mediocre SHG response of  $\text{Cu}_4\text{ZnGe}_2\text{Se}_7$  could be intrinsic to the material, the large Urbach tailing observed in the optical absorption spectrum suggests that the material may be plagued with appreciable defects and/or disorder that could detract from its response. Although  $\text{Cu}_2\text{ZnGeSe}_4$  is non-PM within our experimental range, it may be PM at longer wavelengths into the far-IR. While its relatively narrow bandgap precludes use in high-powered laser applications,  $\text{Cu}_2\text{ZnGeSe}_4$  is a good candidate material for low-powered NLO applications due to its high  $\chi^{(2)}$  value of  $43 \pm 6$  pm/V, which exceeds that of several commercially available IR-NLO crystals, for example  $\text{LiInS}_2$ ,  $\text{LiInSe}_2$ ,  $\text{LiGaS}_2$ ,  $\text{LiGaSe}_2$ , and  $\text{AgGaS}_2$  [99]. Our work here demonstrates that it is likely worthwhile to reinvestigate other long-known DLSs that have not been studied in terms of their NLO properties.

#### Acknowledgements

This work was primarily supported by the United States National Science Foundation under grant numbers DMR-1201729 and DMR-1611198. Funds to purchase the single crystal and powder X-ray diffractometers were received from the United States National Science Foundation under grant numbers CHE-0234872 and DUE-0511444, respectively. Use of the Advanced Photon Source at Argonne National Laboratory was supported by the U. S. Department of Energy, Office of Science, Office of Basic Energy Sciences, under Contract No. DE-AC02-06CH11357. F.O.S. acknowledges support from the Kenya Education Network (KENET) through the Computational Modeling and Materials Science (CMMS) research grant. J.I.J acknowledges the support from the Basic Science Research Programs through the National Research Foundation of Korea (NRF), (2017R1D1A1B03035539 and 2020R1F1A1069646), funded by the Korean government. The authors acknowledge G&H Cleveland for providing the optical-quality  $\text{AgGaSe}_2$  single crystal reference material.

- 
- [1] F.K. Hopkins, Military laser applications: Providing focus to nonlinear optics R&D, *Optics and Photonics News* 9 (1998) 32-38. <https://doi.org/10.1364/OPN.9.2.000032>.
- [2] M.W. Todd, R.A. Provencal, T.G Owano, B.A. Paldus, A. Kachanov, K.L. Vodopyanov, M. Hunter, S.L. Coy, J.I. Steinfeld, J.T. Arnold, Application of mid-infrared cavity-ringdown spectroscopy to trace explosives vapor detection using a broadly tunable (6-8  $\mu\text{m}$ ) optical parametric oscillator, *Appl. Phys. B.* 75 (2002) 367-376. <https://doi.org/10.1007/s00340-002-0991-8>.
- [3] G. Stoepler, M. Eichhorn, M. Schellhorn, S. L. Been, and R. M. Verdaasdonk, "ZGP RISTRA OPO operating at 6.45  $\mu\text{m}$  and application in surgery," in *Lasers, Sources, and Related Photonic Devices*, OSA Technical Digest (CD) (Optical Society of America, 2012), paper AM1A.5. <https://doi.org/10.1364/ASSP.2012.AM1A.5>.
- [4] U. Chatterjee, Development of coherent tunable source in 2-16  $\mu\text{m}$  region using nonlinear frequency mixing process, *Pramana – J. Phys.* 82 (2014) 29-38. <https://doi.org/10.1007/s12043-013-0640-2>.
- [5] Yu.M. Andreev, P.P. Geiko, G.M. Krekov, O.A. Romanovskii, Detection of trace concentration of some simple pollutants in Tomsk, *SPIE Proceedings Vol. 1811 Tenth All-Union Symposium and School on High-Resolution Molecular Spectroscopy* (1991) 367-370. <https://doi.org/10.1117/12.131180>.
- [6] A.G. Jackson, M.C. Ohmer, MC, S.R. LeClair, Relationship of the second order nonlinear optical coefficient to energy gap in inorganic non-centrosymmetric crystals. *Infrared Phys. Technol.* 38 (1997) 233–244. [https://doi.org/10.1016/S1350-4495\(97\)00017-0](https://doi.org/10.1016/S1350-4495(97)00017-0).
- [7] M.C. Ohmer, R. Pandey, Emergence of chalcopyrites as nonlinear optical materials, *MRS Bull.* 23 (1998) 16-22. <https://doi.org/10.1557/S0883769400029031>.
- [8] P.G. Schunemann, Improved NLO crystals for mid-IR laser applications, *Proc. SPIE* 6455, *Nonlinear Frequency Generation and Conversion: Materials, Devices and Applications, VI*, 64550R (14 February 2007). <https://doi.org/10.1117/12.701504>.
- [9] I.B. Zotova, Y.J. Ding, Optical parametric oscillators in the presence of strong two-photon absorption for extended applications of nonlinear optical materials, *Opt. Commun.* 198 (2001) 453–458. [https://doi.org/10.1016/S0030-4018\(01\)01543-7](https://doi.org/10.1016/S0030-4018(01)01543-7).
- [10] G.C. Catella, D. Burlage, Crystal growth and optical properties of  $\text{AgGaS}_2$  and  $\text{AgGaSe}_2$ , *MRS Bull.* 23 (1998) 28–36. <https://doi.org/10.1557/S0883769400029055>.
- [11] M.-C. Chen, L.-M. Wu, H. Lin, L.-J. Zhou, L. Chen, Disconnection enhances the second harmonic generation response: Synthesis and characterization of  $\text{Ba}_{23}\text{Ga}_8\text{Sb}_2\text{S}_{38}$ , *J. Am. Chem. Soc.* 134 (2012) 6058-6060. <https://doi.org/10.1021/ja300249n>.
- [12] Z.-Z. Luo, C.-S. Lin, W.-D. Cheng, H. Zhang, W.-L. Zhang, Z.-Z. He, Syntheses, Characterization, and optical properties of ternary Ba-Sn-S system compounds: Acentric  $\text{Ba}_7\text{Sn}_4\text{S}_{15}$ , centric  $\text{BaSn}_2\text{S}_5$  and centric  $\text{Ba}_6\text{Sn}_7\text{S}_{10}$ , *Inorg. Chem.* 52 (2013) 273-279. <https://doi.org/10.1021/ic301804n>.
- [13] I. Chung, M.G. Kanatzidis, Metal chalcogenides: A rich source of nonlinear optical materials, *Chem Mater.* 26 (2014) 849-869. <https://doi.org/10.1021/cm401737s>.
- [14] J.A. Aitken, J.A. Brant, D.J. Clark, Y.S. Kim, J.I. Jang, J. I., Impact of bandgap on infrared optical nonlinearity in novel quaternary chalcogenides:  $\text{Cu}_2\text{CdSnS}_4$ ,  $\alpha/\beta\text{-Cu}_2\text{ZnSiS}_4$  and

- 
- $\text{Li}_2\text{CdGeS}_4$ , in: F. Wilkins (Ed.), *Nonlinear Optics: Fundamentals, Applications and Technological Advances*, Nova Science Publishers Inc., New York, 2014, pp. 1-61.
- [15] S.A. Avanesov, D.V. Badikov, V.V. Badikov, V.L. Panyutin, V. Petrov, G.S. Shevyrdayeva, A.A. Martynov, K.V. Mitin, Phase equilibrium studies in the  $\text{PbTe-Ga}_2\text{Te}_3$  and  $\text{PbTe-In}_2\text{Te}_3$  systems for growing new nonlinear optical crystals of  $\text{PbGa}_6\text{Te}_{10}$  and  $\text{PbIn}_6\text{Te}_{10}$  with transparency extending into the far-IR, *J. Alloy Compd.* 612 (2014) 386-391. <https://doi.org/10.1016/j.jallcom.2014.05.168>.
- [16] Z.-Z. Luo, C.-S. Lin, H.-H. Cui, W.-L. Zhang, H. Zhang, H. Chen. Z.-Z. He, W.-D. Cheng,  $\text{PbGa}_2\text{MSe}_6$  (M=Si, Ge): Two exception infrared nonlinear optical crystals, *Chem. Mater* 27 (2015) 914-922. <https://doi.org/10.1021/cm504195x>.
- [17] W. Khan, G. Murtaza, T. Ouahrani, A. Mahmood, R. Khenata, M. El Amine Monir, H. Baltache, Electronic, bonding, linear and non-linear optical properties of novel  $\text{Li}_2\text{Ga}_2\text{GeS}_6$  compound, *J. Alloy Compd.* 2016, 674, 109-115. <https://doi.org/10.1016/j.jallcom.2016.02.213>.
- [18] W. Yin, A.K. Iyer, C. Li, J. Yao, A. Mar, Noncentrosymmetric chalcogenides  $\text{BaZnSiSe}_4$  and  $\text{BaZnGeSe}_4$  features one-dimensional structures, *J. Alloy Compd.* 708 (2017) 414-421. <https://doi.org/10.1016/j.jallcom.2017.03.009>.
- [19] S.-P. Guo, Y. Chi, G.-C. Guo, Recent achievement on middle and far-infrared second-order nonlinear optical materials. *Coordin. Chem. Rev.* 335 (2017) 44-57. <https://doi.org/10.1016/j.ccr.2016.12.013>.
- [20] F. Liang, L. Kang, Z. Lin, Y. Wu, Mid-infrared nonlinear optical materials based on metal chalcogenides: Structure-property relationship, *Cryst. Growth Des.* 17 (2017) 2254-2289. <https://doi.org/10.1021/acs.cgd.7b00214>.
- [21] O.Y. Khyzhun, V.S. Babizhetskyy, I.V. Kityk, G.L. Myronchuk, J. Jędryka, G. Lakshminarayana, V.O. Levytskyy, O.V. Tsisar, L.V. Piskach, O.V. Parasyuk, A.M. El Naggari, A.A. Albassam, M. Piasecki, Thallium indium germanium sulphide ( $\text{TlInGe}_2\text{S}_6$ ) as efficient material for nonlinear optical application, *J. Alloy Compd.* 735 (2018) 1694-1702. <https://doi.org/10.1016/j.jallcom.2017.11.257>.
- [22] K. Wu, S. Pan, A review on structure-performance relationship toward the optimal design of infrared nonlinear optical materials with balanced performances, *Coordin. Chem. Rev.* 377 (2018) 191-208. <https://doi.org/10.1016/j.ccr.2018.09.002>.
- [23] H. Xia, Q. Ma, Experimental study on nonlinear-optical property of  $\text{Ag}_4\text{P}_2\text{Se}_6$ , *J. Alloy Compd.* 780 (2019) 727-733. <http://doi.org/10.1016/j.jallcom.2018.11.403>.
- [24] K. Wu, Y. Chu, Z. Yang, S. Pan,  $\text{A}_2\text{SrM}^{\text{IV}}\text{S}_4$  (A = Li, Na;  $\text{M}^{\text{IV}}$  = Ge, Sn) concurrently exhibiting wide bandgaps and good nonlinear optical responses as new potential infrared nonlinear optical materials, *Chem. Sci.* 10 (2019) 3963-3968. <https://doi.org/10.1039/c9sc00028c>.
- [25] E. Parthé, *Crystal Chemistry of Tetrahedral Structures*, Gordon and Breach Science Publishers, New York, NY, 1964.
- [26] N.A. Goryunova, *The Chemistry of Diamond-Like Semiconductors*, in: J.C. Anderson (Ed.) The MIT Press, Cambridge (UK), 1965.
- [27] B. Pamplin, The adamantine family of compounds, *Prog. Crystal Growth Charact.* 3 (1980) 179-192. [https://doi.org/10.1016/0146-3535\(80\)90018-0](https://doi.org/10.1016/0146-3535(80)90018-0).
- [28] C.D. Brunetta, J.A. Brant, K.A. Rosmus, K.M. Henline, E. Karey, J.H. MacNeil, J.A. Aitken, The impact of three new quaternary sulfides on the current predictive tools for structure

- 
- and composition of diamond-like materials, *J. Alloy Compd.* 574 (2013) 495-503. <https://doi.org/10.1016/j.jallcom.2013.05.141>.
- [29] J.A. Brant, D.J. Clark, Y.S. Kim, J.I. Jang, A. Weiland, J.A. Aitken, Outstanding laser damage threshold in  $\text{Li}_2\text{MnGeS}_4$  and tunable optical nonlinearity in diamond-like semiconductors, *Inorg. Chem.* 54 (2015) 2809-2819. <https://doi.org/10.1021/ic502981r>.
- [30] G. Li, Y. Chu, Z. Zhou, From  $\text{AgGaS}_2$  to  $\text{Li}_2\text{ZnSiS}_4$ : Realizing impressive high laser damage thresholds together with large second-harmonic generation response. *Chem. Mater.* 30 (2018) 602-606. <https://doi.org/10.1021/acs.chemmater.7b05350>.
- [31] J.-H. Zhang, D.J. Clark, J.A. Brant, K.A. Rosmus, P. Grima, J.W. Lekse, J.I. Jang, J.A. Aitken,  $\alpha\text{-Li}_2\text{ZnGeS}_4$ : A wide-bandgap diamond-like semiconductor with excellent balance between laser-induced damage threshold and second harmonic generation response, *Chem. Mater.* 32 (2020) 8947-8955. <https://dx.doi.org/10.1021/acs.chemmater.0c02929>
- [32] Y. Huang, K. Wu, J. Cheng, Y. Chu, Z. Yang, S. Pan,  $\text{Li}_2\text{ZnGeS}_4$ : a promising diamond-like infrared nonlinear optical material with high laser damage threshold and outstanding second harmonic generation response, *Dalton Trans.* 48 (2019) 4484-4488. <https://doi.org/10.1039/C9DT00269C>
- [33] J.-H. Zhang, S.S. Stoyko, A.J. Craig, P. Grima, J.W. Kotchey, J.I. Jang, J.A. Aitken, Phase matching, strong frequency doubling and outstanding laser-induced damage threshold in the biaxial, quaternary diamond-like semiconductor  $\text{Li}_4\text{CdSn}_2\text{S}_7$ , *Chem. Mater* 32 (2020) 10045-10054. <https://dx.doi.org/10.1021/acs.chemmater.0c03268>
- [34] G.-M. Li, Y. Chu, J. Li, Z.-X. Zhou,  $\text{Li}_2\text{CdSiS}_4$ , a promising IR NLO material with balanced Eg and SHG response originating from the effect of Cd with  $d^{10}$  configuration, *Dalton Trans.* 49 (2020) 1975-1980.
- [35] J.A. Brant, D.J. Clark, Y.S. Kim, J.I. Jang, J.-H. Zhang, J.A. Aitken,  $\text{Li}_2\text{CdGeS}_4$ , A diamond-like semiconductor with strong second-order optical nonlinearity in the infrared and exceptional laser damage threshold, *Chem. Mater.* 26 (2014) 3045-3048. <https://doi.org/10.1021/cm501029s>.
- [36] K. Wu, S. Pan,  $\text{Li}_2\text{HgMS}_4$  (M=Si, Ge, Sn): New quaternary diamond-like semiconductors for infrared laser frequency conversion. *Crystals* 7 (2017) 107. <https://doi.org/10.3390/cryst7040107>.
- [37] K. Wu, Z. Yang, S. Pan, The first quaternary diamond-like semiconductor with 10-membered  $\text{LiS}_4$  rings exhibiting excellent nonlinear optical performances, *Chem. Comm.* 53 (2017) 3010-3013. <https://doi.org/10.1039/C6CC09565H>.
- [38] H. Hahn, H. Schulze, Über quaternäre Chalkogenide des germaniums und zinn, *Naturwissenschaften* 52 (1965) 426. <https://doi.org/10.1007/BF00589678>.
- [39] R. Nitsche, D.F. Sargent, P. Wild, Crystal growth of quaternary  $1_2246_4$  chalcogenides by iodine vapor transport, *J. Cryst. Growth* 1 (1967) 52-53. [https://doi.org/10.1016/0022-0248\(67\)90009-7](https://doi.org/10.1016/0022-0248(67)90009-7).
- [40] L. Shi, P. Yin, Phosphate-free synthesis, optical absorption and photoelectric properties of  $\text{Cu}_2\text{ZnGeS}_4$  and  $\text{Cu}_2\text{ZnGeSe}_4$  uniform nanocrystals, *Dalton Trans.* 42 (2013) 13607-13611. <https://doi.org/10.1039/C3DT50993A>.
- [41] L. Choubrac, G. Brammertz, N. Barreau, L. Arzel, S. Harel, M. Meuris, B. Vermang, 7.6% CZGSe solar cells thanks to optimized CdS chemical bath deposition, *Phys. Stat. Sol. A*, 215, 1800043. <https://doi.org/10.1002/pssa.201800043>.

- 
- [42] M. Ibáñez, R. Zamani, A. LaLonde, D. Cadavid, W. Li, A. Shavel, J. Arbiol, J.R. Morante, S. Gorsse, G.J. Synder, A. Cabot, Cu<sub>2</sub>ZnGeSe<sub>4</sub> nanocrystals: Synthesis and thermoelectric properties, *J. Am. Chem. Soc.* 134 (2012) 4060-4063. <https://doi.org/10.1021/ja211952z>.
- [43] W.G. Zeier, Y. Pei, G. Pomrehn, T. Day, N. Heinz, C.P. Heinrich, G.J. Synder, W. Tremel, Phonon Scattering through a local anisotropic structural disorder in the thermoelectric solid solution Cu<sub>2</sub>Zn<sub>1-x</sub>Fe<sub>x</sub>GeSe<sub>4</sub>, *J. Am. Chem. Soc.* 135 (2013) 726-732. <https://doi.org/10.1021/ja308627v>.
- [44] W. Schäfer, K. Scheunemann, R. Nitsche, Crystal structure and magnetic properties of Cu<sub>4</sub>NiSi<sub>2</sub>S<sub>7</sub>, *Mater. Res. Bull.* 15 (1980) 933-937. [https://doi.org/10.1016/0025-5408\(80\)90218-4](https://doi.org/10.1016/0025-5408(80)90218-4).
- [45] L.D. Gulay, I.D. Olekseyuk, O.V. Parasyuk, Crystal structures of the Ag<sub>4</sub>HgGe<sub>2</sub>S<sub>7</sub> and Ag<sub>4</sub>CdGe<sub>2</sub>S<sub>7</sub> compounds, *J. Alloy Compd.* 340 (2002) 157-166. [https://doi.org/10.1016/S0925-8388\(02\)00016-6](https://doi.org/10.1016/S0925-8388(02)00016-6).
- [46] T. Kaib, S. Haddadpour, H.F. Andersen, L. Mayrhofer, T.T. Järvi, M. Moseler, K.-C. Möller, S. Dehnen, Quaternary diamond-like chalcogenidometalate networks as efficient anode materials in lithium-ion batteries, *Adv. Funct. Mater.* 23 (2013) 5693-5699. <https://doi.org/10.1002/adfm.201301025>.
- [47] Y. Guo, F. Liang, Z. Li, W. Xing, Z. Lin, J. Yao, Y. Wu, Li<sub>4</sub>HgSn<sub>2</sub>Se<sub>7</sub>: The first second-order nonlinear optical-active selenide in the I<sub>4</sub>-II-IV<sub>2</sub>-VI<sub>7</sub> diamond-like family, *Cryst. Growth Des.* 19 (2019) 5494-5497. <https://doi.org/10.1021/acs.cgd.9b01074>
- [48] A.J. Craig, S.S. Stoyko, A. Bonnoni, J.A. Aitken, Synthesis and crystal structure of the quaternary thiogermanates Cu<sub>4</sub>FeGe<sub>2</sub>S<sub>7</sub> and Cu<sub>4</sub>CoGe<sub>2</sub>S<sub>7</sub>, *Acta Cryst E* 76 (2020) 1117-1121. <https://doi.org/10.1107/S2056989020007872>.
- [49] S. Nakamura, T. Maeda, T. Wada, Phase stability and electronic structure of In-free photovoltaic materials: Cu<sub>2</sub>ZnSiSe<sub>4</sub>, Cu<sub>2</sub>ZnGeSe<sub>4</sub> and Cu<sub>2</sub>ZnSnSe<sub>4</sub>. *Jpn. J. Appl. Phys.* 49, 121203. <https://doi.org/10.1143/JJAP.49.121203>.
- [50] D. Chen, N.M. Ravindra, Electronic and optical properties of Cu<sub>2</sub>ZnGeX<sub>4</sub> (X=S, Se and Te) quaternary semiconductors, *J. Alloy Compd.* 579 (2013) 468-472. <https://doi.org/10.1016/j.jallcom.2013.06.048>.
- [51] O.Y. Khyzhun, V.L. Bekenev, V.A Ocheretova, A.O. Fedorchuk, O.V. Parasyuk, Electronic structure of Cu<sub>2</sub>ZnGeSe<sub>4</sub> single crystal: Ab initio FP-LAPW calculations and X-ray spectroscopy measurements, *Physica B* 461 (2015) 75-84. <https://doi.org/10.1016/j.physb.2014.12.016>.
- [52] S.G. Choi, J.-S. Park, A. L. Donohue, S.T. Christensen, B. To, C. Beall, S.-H. Wei, I.L. Repins, Electronic Structure and Optical Properties of Cu<sub>2</sub>ZnGeSe<sub>4</sub>: First-principles calculations and vacuum-ultraviolet spectroscopic ellipsometric studies. *Phys Rev. Applied.* 4, 054006. <https://doi.org/10.1103/PhysRevApplied.4.054006>.
- [53] Bruker (2012). APEX2, SMART, SAINT. Bruker AXS Inc., Madison, Wisconsin, USA.
- [54] (a) Sheldrick, G. M. (1996). SADABS. University of Göttingen, Germany. (b) G. M. Sheldrick, Crystal structure refinement with SHELXL, *Acta Cryst.* C71 (2015) 3-8. <https://doi.org/10.1107/S2053229614024218>
- [55] J. Wang, B. H. Toby, P. L. Lee, L. Ribaud, S. M. Antao, C. Kurtz, M. Ramanathan, R. B. Von Dreele, M. A. Beno, A dedicated powder diffraction beamline at the Advanced Photon

- 
- Source: Commissioning and early operational results, *Rev. Sci. Instru.* 79 (2008) 085105.  
<https://doi.org/10.1063/1.2969260>
- [56] A. A. Coelho, TOPAS and TOPAS-Academic: an optimization program integrating computer algebra and crystallographic objects written in C++, *J. Appl. Cryst.* 51 (2018) 210-218.  
<https://doi.org/10.1107/S1600576718000183>
- [57] O.V. Parasyuk, L.D. Gulay, Ya.E. Romanyuk, L.V. Piskach, Phase diagram of the  $\text{Cu}_2\text{GeSe}_3$ - $\text{ZnSe}$  system and crystal structure of the  $\text{Cu}_2\text{ZnGeSe}_4$  compound, *J. Alloy Compd.* 329 (2001) 202-207. [https://doi.org/10.1016/S0925-8388\(01\)01606-1](https://doi.org/10.1016/S0925-8388(01)01606-1).
- [58] G. Gurieva, D.M. Töbrens, M. Ya. Valakh, S. Schorr, Cu-Zn disorder in  $\text{Cu}_2\text{ZnGeSe}_4$ : A complementary neutron diffraction and Raman spectroscopy study, *J. Phys. Chem. Sol.* 99 (2016) 100-104. <https://doi.org/10.1016/j.jpcs.2016.08.017>.
- [59] (a) P. Kubelka, F. Munk, Ein Beitrag Zur Optik Der Farbanstriche, *Z. Technol. Phys.* 12 (1931) 593–601. (b) An article on optics of paint layers: an English translation of the Kubelka Munk paper by S. Westin.  
<http://www.graphics.cornell.edu/~westin/pubs/kubelka.pdf>, 2004 (accessed 12 June 2020).
- [60] F. Urbach, The long-wavelength edge of photographic sensitivity and of the electronic absorption of solids, *Phys. Rev.* 92 (1953) 1324. <https://doi.org/10.1103/PhysRev.92.1324>.
- [61] R. J. McGowan, Attenuated total reflectance vs. transmission infrared spectroscopy in the quantitative evaluation of paint vehicles, *Anal. Chem.* 35, (1963) 1664-1665.  
<https://doi.org/10.1021/ac60204a037>.
- [62] S. Kurtz, T. Perry, A powder technique for the evaluation of nonlinear optical materials, *J. Appl. Phys.* 39 (1968) 3798-3813. <https://doi.org/10.1063/1.1656857>.
- [63] J.C. Syrigos, D.J. Clark, F.O. Saouma, S.M. Clarke, L. Fang, J.I. Jang, M.G. Kanatzids, Semiconducting properties and phase-matching nonlinear optical response of the one-dimensional selenophosphates  $\text{ANb}_2\text{PSe}_{10}$  (A=K, Rb and Cs), *Chem. Mater* 27 (2014) 255-265. <https://doi.org/10.1021/cm5038217>.
- [64] S.J. Clark, M.D. Segall, C.J. Pickard, P.J. Hasnip, M.J. Probert, K. Refson, M.C. Payne, First principles methods using CASTEP, *Z. Kristallogr.* 220 (2005) 567-570.  
<https://doi.org/10.1524/zkri.220.5.567.65075>.
- [65] W. Kohn, L.J. Sham, Self-consistent equations including exchange and correlations effects, *Phys. Rev.* 140 (1965) A1133-A1138. <https://doi.org/10.1103/PhysRev.140.A1133>.
- [66] J.P. Perdew, M. Burke, M. Ernzerhof, Generalized gradient approximation made simple, *Phys. Rev. Lett.* 77 (1996) 3865-3868. <https://doi.org/10.1103/PhysRevLett.77.3865>.
- [67] J.S. Lin, A. Qteish, M.C. Payne, V. Heine, Optimized and transferable nonlocal separable ab initio pseudopotentials, *Phys. Rev. B* 47 (1993) 4174-4180.  
<https://doi.org/10.1103/PhysRevB.47.4174>.
- [68] D.M. Schleich, A. Wold, Optical and Electrical properties of quaternary chalcogenides, *Mat. Res. Bull.* 12 (1977) 111-114. [https://doi.org/10.1016/0025-5408\(77\)90150-7](https://doi.org/10.1016/0025-5408(77)90150-7).
- [69] C.-I. Lee, C.-D. Kim, Optical properties of undoped and  $\text{Co}^{2+}$ -doped  $\text{Cu}_2\text{ZnGeSe}_4$  crystals, *J. Korean. Phys. Soc.* 37 (2000) 364-367.
- [70] H. Matsushita, T. Ichikawa, A. Katsui, Structural, thermodynamical and optical properties of  $\text{Cu}_2\text{-II-IV-VI}_4$  quaternary compounds, *J. Mater. Sci.* 40 (2005) 2003-2005.  
<https://doi.org/10.1007/s10853-005-1223-5>.

- 
- [71] P.U. Bhaskar, G.S. Babu, Y.B.K. Kumar, V.S. Raja, Preparation and characterization of co-evaporated  $\text{Cu}_2\text{ZnGeSe}_4$  thin films, *Thin Solid Films* 534 (2013) 249-254. <https://doi.org/10.1016/j.tsf.2013.03.001>.
- [72] M. Guc, S. Levchenko, V. Izquierdo-Roca, X. Fontané, E. Arushanov, A. Pérez-Rodríguez, Polarized Raman scattering analysis of  $\text{Cu}_2\text{ZnSnSe}_4$  and  $\text{Cu}_2\text{ZnGeSe}_4$  single crystals, *J. Appl. Phys.* 114 (2013) 193514. <https://doi.org/10.1063/1.4830028>.
- [73] R.W.G. Wyckoff, *Crystal Structures*, second ed., Interscience Publishers, New York, New York, 1963.
- [74] L. Pauling, The principles determining the structure of complex ionic crystals, *J. Am. Chem. Soc.* 51 (1929) 1010–1026. <https://doi.org/10.1021/ja01379a006>.
- [75] S. Schorr, H.J. Hoebler, M. Tovar, *Eur. J. Mineral.* 19 (2007) 65-73. <https://doi.org/10.1127/0935-1221/2007/0019-0065>
- [76] S. Schorr, The crystal structure of kesterite type compounds, A neutron and X-ray diffraction study, *Sol. Energy Mater. Sol. Cells*, 95 (2011) 1482-1488. <https://doi.org/10.1016/j.solmat.2011.01.002>.
- [77] A. Lafond, L. Choubrac, C. Guillot-Deudon, P. Deniard, S. Jobic, Crystal structures of photovoltaic chalcogenides, an intricate puzzle to solve: the cases of CIGSe and CZTS materials, *Z. Anorg. Allg. Chem.* 638 (2012) 2571-2577. <https://doi.org/10.1002/zaac.201200279>.
- [78] S. Schorr, Crystallographic Aspects of CZTS, in: Kentaro Ito (Ed.), *Copper Zinc Tin Sulfide-Based Thin Film Solar Cells*, Wiley, 2015, pp. 55-74.
- [79] I. D. Brown, *The Chemical Bond in Inorganic Chemistry The Bond Valence Model*, Second Edition, Oxford University Press, Oxford, United Kingdom 2016.
- [80] I. D. Brown, Modelling the structures of  $\text{La}_2\text{NiO}_4$ . *Z. Kristallog.* 199 (1992) 255-272. <https://doi.org/10.1524/zkri.1992.199.3-4.255>
- [81] I. D. Brown, D. Altermatt, Bond-valance parameters obtained from a systematic analysis of the Inorganic Crystal Structure Database, *Acta. Cryst.* B41 (1985) 244-247. <https://doi.org/10.1107/S0108768185002063>
- [82] M. O’Keeffe, A method calculating bond valences in crystals, *Acta Cryst.* 46A (1990) 138-142. <https://doi.org/10.1107/S0108767389011104>
- [83] [https://www.iucr.org/\\_\\_data/assets/file/0011/150779/bvparm2020.cif](https://www.iucr.org/__data/assets/file/0011/150779/bvparm2020.cif)
- [84] A. Salinas-Sanchez, J. L. Garcia-Muñoz, J. Rodriguez-Carvajal, R. Saez-Puche, J. L. Martinez, Structural characterization of  $\text{R}_2\text{BaCuO}_5$  (R=Y, Yb, Tm, Er, Ho, Dy, Gd, Eu and Sm) oxides by X-ray and neutron diffraction, *J. Solid State. Chem.* 100 (1992) 201-211. [https://doi.org/10.1016/0022-4596\(92\)90094-C](https://doi.org/10.1016/0022-4596(92)90094-C)
- [85] M. E. Fleet, Structure transformations in natural ZnS, *Am. Min.* 62 (1977) 540-546.
- [86] E. Parthé, E., *Elements of Inorganic Structural Chemistry: Selected Efforts to Predict Structural Factors*, 2 ed, K. Sutter Parthé Publisher, Lancy, Switzerland, 1996.
- [87] A. Dugarte-Dugarte, N. Ramirez Pineda, L. Nieves, J. A. Henao, G. Diaz de Delgado, J. M. Delgado, The crystal structure of  $\text{Cu}_2\text{GeSe}_3$  and the structure-types of the  $\text{I}_2\text{-IV-VI}_3$  family of semiconducting compounds, *Acta Cryst.* B77, (2021) 158-167. <https://doi.org/10/1107/S2052520620016571>.

- 
- [88] O. M. Strok, I. D. Olekseyuk, O. F. Zmiy, I. A. Ivashchenko, L. D. Gulay, The quasi-ternary system  $\text{Cu}_2\text{Se-Ga}_2\text{Se}_3\text{-GeSe}_2$ , *J. Phase Equilibria Diffus* 34 (2013) 94-103.  
<https://doi.org/10.1007/s11669-013-0188-3>
- [89] M. P. Kulakov, V. D. Kulakovskii, I. B. Savchenko, A. V. Fadeev, Phase transition in zinc selenide crystals, *Sov Phys. Solid State* 18 (1976) 526-527.
- [90] E. Parthé, J. Garin, Zinkblende- und Wurtzitüberstrukturen bei ternären Chalkogeniden der Zusammensetzung  $1_246_3$ , *Monatsh. Chem.* 102 (1971) 1197-1208.  
<https://doi.org/10.1007/BF00917173>
- [91] J. Rivet, Contribution a l'etude de quelques combinaisons ternaires sulfurees, selenies ou tellurees du cuivre avec les elements du groupe IV, *Ann. Chim. Fr.*, 10 (1965) 243-270.
- [92] A.C. Malingowski, P.W. Stephens, A. Huq, Q. Huang, S. Khalid, P.G. Khalifah, Substitutional mechanism of Ni into the wide-band-gap semiconductor  $\text{InTaO}_4$  and its implications for water splitting activity in the wolframite structure type, *Inorg. Chem.* 51 (2012) 6096-6103. <https://doi.org/10.1021/ic202715c>.
- [93] J. I. Pankove, *Optical processes in semiconductors*, Dover Publications, New York, 1971.
- [94] B. Choudhury, M. Dey, A. Choudhury, 2013, Defect generation, d-d transition, and band gap reduction in Cu-Doped  $\text{TiO}_2$  nanoparticles. *Int. Nano Lett.* 3, 25.  
<https://doi.org/10.1186/2228-5326-3-25>.
- [95] M. Buffière, H. ElAnzeery, S. Oueslati, K. Ben Messaoud, G. Brammertz, M. Meuris, J. Poortmans, Physical characterization of  $\text{Cu}_2\text{ZnGeSe}_4$  thin films from annealing of Cu-Zn-Ge precursor layers, *Thin Solid Films* 582 (2015) 171-175.  
<https://doi.org/10.1016/j.tsf.2014.09.024>.
- [96] M. Larciprete, D. Haertle, A. Belardini, M. Bertolotti, F. Sarto, P. Günter, Characterization of second and third order optical nonlinearities of ZnO sputtered films, *Appl. Phys.* 82B (2006) 431-437. <https://doi.org/10.1007/s00340-005-2022-z>.
- [97] H.P. Wagner, M. Kühnelt, W. Langbein, J.M. Hvam, Dispersion of the second-order nonlinear susceptibility in ZnTe, ZnSe and ZnS, *Phys. Rev. B*, 58 (1998) 10494.  
<https://doi.org/10.1103/PhysRevB.58.10494>.
- [98] A. S. Haynes, F. O. Saouma, C. O. Otieno, D. J. Clark, D. P. Shoemaker, J. I. Jang and M. G. Kanatzidis, *Chem. Mater.* 27 (2015) 1837-1846.
- [99] D. N. Nikogosyan, *Nonlinear optical crystals: a complete survey*. (Springer Science & Business Media, 2006).